Illuminating the Darkness: Using Alternative Parameterizations to Test Dark Energy Properties

by
Eduardo J. Ruiz

A dissertation submitted in partial fulfillment
of the requirements for the degree of
Doctor of Philosophy
(Physics)
in the University of Michigan
2014

Doctoral Committee:

Associate Professor Dragan Huterer, Chair
Professor August Evrard
Professor Katherine Freese
Professor David W. Gerdes
Assistant Professor Christopher John Miller

If the whole universe has no meaning, we should never have found out that it has no meaning: just as, if there were no light in the universe and therefore no creatures with eyes, we should never know it was dark. Dark would be without meaning.

- C. S. Lewis, *Mere Christianity*

ACKNOWLEDGEMENTS

Most of the computation for this work was done using the Python programming language and made extensive use of the `numpy` and `scipy` computing packages. A small portion was written in C/C++ using the Numerical Recipes and Gnu Scientific Libraries. All figures were created using the `matplotlib` package for Python. I was supported by a grant from the NSF during the course of this work.

Many people supported me while I did this research and throughout my graduate career. Some who deserve special thanks are:

- Dragan Huterer, for the significant contributions he made for this research, and for being the best advisor during these many years.
- Daniel Shafer, for many insightful conversations in physics and statistical matters, and for teaching me how to make exceptional plots.
- Adam Becker, for introducing me to the wonderful world of Python, and for providing some much-needed guidance in my first years of graduate school.
- Gus Evrard, Katherine Freese, David Gerdes, and Chris Miller for agreeing to serve on my defense committee.
- Richard, Steven, Amanda, and Bill, for the many adventures (and misadventures) we've had together, and for being there in the times when I needed it.

- The Graduate Christian Fellowship, for being the greatest community of graduate students anyone could ask for, and for reminding me to take a break and rest occasionally.

- George and Mary Lindquist, for their hospitality and generosity.

- My parents, Pedro and Madeline, for having raised me to love science and supporting me throughout my entire education, both emotionally and financially.

- My sister, Alexandra, for putting up with my shenanigans, and always making me laugh.

- And to Kristin, for being the most patient and loving wife in the world.

TABLE OF CONTENTS

LIST OF FIGURES

FIGURE **Page**

LIST OF TABLES

TABLE **Page**

LIST OF APPENDICES

APPENDIX **Page**

ABSTRACT

In the first half of my dissertation, I study the effects of type Ia supernova (SNIa) systematic errors on dark energy using current data from the Supernova Legacy Survey. I consider how these systematics affect constraints from combined cosmological probes that include SNIa, baryon acoustic oscillations, and the cosmic microwave background. The temporal evolution of dark energy is described in terms of principal components of the equation of state, though simpler models are examined as well. The SNIa systematics are found to degrade the generalized figure of merit, which characterizes constraints in the multidimensional dark energy parameter space, by a factor of three to four. Nevertheless, overall constraints obtained on more than five principal components are very good with current data, even with the inclusion of known systematics.

In the second half, I perform tests of the consistency of the standard wCDM model in the framework of General Relativity by separating out the information between geometry and growth of structure. Each late-universe dark energy parameter is replaced with two parameters: one describing geometrical information, and the other controlling the growth of structure. I use data from all principal cosmological probes to constrain both geometry and growth; of these, SNIa, baryon acoustic oscillations, and the cosmic microwave background primarily measure geometry, while cluster counts, weak gravitational lensing shear, and redshift space distortions constrain both geometry and growth. Both geometry and growth separately favor the ΛCDM cosmology with the matter density relative to critical $\Omega_M \simeq 0.3$. Allowing

the split equations of state to vary separately results in good agreement with the ΛCDM value ($w \simeq -1$), with the major exception of redshift space distortions which favor less growth than in ΛCDM at $3-\sigma$ confidence, favoring instead $w^{\rm grow} \simeq -0.8$. This preference by redshift space distortions for less growth has been noted previously and may be due to systematics, or be explained by the sum of the neutrino masses higher than that expected from the simplest mass hierarchies, $m_\nu = 0.45$ eV. Even in the new, larger parameter space the constraints are tight due to the impressive complementarity of different cosmological probes.

CHAPTER 1

An Introduction to Dark Energy

1.1 The Accelerated Expansion of the Universe

The discovery of the accelerated expansion of the universe in 1998 [62, 65] was a major and unexpectd paradigm shift in cosmology. Since then, there have been many people working on this mystery, trying to understand what is causing it, and to learn its properties.

The acceleration is generally attributed to dark energy (DE), a mysterious repulsive force that acts on the largest scales in the universe, driving all things apart. The nature of DE is, however, a complete mystery. The most widely accepted model is that of the cosmological constant, denoted ΛCDM (where Λ refers to the cosmological constant and CDM refers to cold dark matter, another necessary ingredient for this model). In this model a constant term in Einstein's equations gives rise to this acceleration, most often attributed to the vacuum energy of space itself.

There are many other models that try to expand on the idea of the cosmological constant: quintessence models, for example, introduce a uniform scalar field that permeates the universe. This scalar field is what causes the expansion, leading to similar effects predicted by ΛCDM. However, unlike the cosmological constant, the scalar field is dynamical, and has an equation of state $w = p/\rho$ (where p is the pressure associated with dark energy and ρ its energy density) different than that of Λ. The

scalar field dynamics dictates how the energy density of the field varies as a function of scale factor. Within the ΛCDM model, the equation of state has a value of $w = -1$, leading to exponential growth. With a scalar field this quantity can take on a variety of values, and even itself change as a function of time. Determining these properties of the DE has been the goal of many researchers, as knowing them can give us insight to the nature of DE.

However, there are alternate theories that also attempt to explain the acceleration of the expansion without the introduction of a new mysterious force. Many of these theories achieve this by altering the equations that govern the gravitational interactions between massive bodies. In these theories, the force of gravity is scale-dependent, that is, the strength and nature of gravity can change from solar-system and galaxy scales to scales the size of the universe. The exact methods in which this is accomplished differ between specific models (for an excellent review of models of modified gravity, see Reference [46]), but they all lead to the same effect: a repulsive force that is responsible for the expansion of the universe on the largest scales while that same force is screened in some manner at cluster-sized scales and below.

Because the acceleration of the universe started relatively recently, any explanations have to be able to explain the cause of the acceleration as a function of time. DE provides this explanation with ease: because the energy density of other constituents of the universe (such as matter and radiation) decreases as the universe expands, the constant (or nearly constant, in the case of non-Λ DE) energy density of DE implies that its fraction of the total energy density of the universe increases as a function of time. This in turn means that for the late universe, the effects of DE become more prominent, whereas in the early universe, they are virtually nonexistent. These two different eras of time (the early universe which is mostly radiation and matter dominated, and the DE-dominated late universe) provide us with the ability to test different aspects of DE, whether it be finding out how different systematics can affect

the constraints on the various cosmological parameters or figuring out if the various effects attributed to dark energy give consistent results to these parameter values.

1.2 Cosmological Distance and Growth

Dark energy influences two main aspects of the universe; as mentioned before, it is thought to be directly responsible for the acceleration of the expansion of the universe, and thus the distances involved between objects in the universe. DE is also understood to influence the rate of structure formation in the universe, since the expansion also affects how quickly matter can clump together and form the large structures in the universe, such as galaxies and clusters of galaxies. In the following subsections, I will give a brief overview of the equations that form a basis for the probes described in Chapter 2. These equations can be broadly split into two categories: those that determine cosmological distances and the geometry of the universe, and those that describe the growth of structure, a distinction that will be useful in Chapter 4.

1.2.1 The Hubble Parameter and the Comoving Distance

Measuring cosmological distances is a tricky task; as the universe expands, the coordinates that we use to measure distances expand along with it. Fortunately, there ways to take the expansion into account. If we assume that the universe is homogeneous and isotropic, we can use the Friedmann-Robertson-Walker (FRW) metric

$$ds^2 = dt^2 - a^2(t)\left(\frac{dr^2}{1-kr^2} + r^2 d\Omega\right), \tag{1.1}$$

where k is the curvature of the universe, assumed to be $k = 0$ (flat universe) throughout this work. The FRW metric also introduces the scale factor $a(t)$. The scale factor measures the amount the universe has grown after a certain amount of time t, and is defined to be $a(t = t_0) = a_0 = 1$ today.

A useful relation is how the scale factor is related to redshift z

$$a = \frac{1}{1+z}. \tag{1.2}$$

This relation allows us to measure the redshift of a distant object and determine how large the universe would have been at the time. This in turn provides us with the age of the object when it emitted the light used to measure the redshift. Because of this relation, these two parameters (a and z) will be used interchangeably throughout this work.

Because we have assumed homogeneity and isotropy, the universe will expand uniformly. A uniformly expanding universe is described by the Hubble Law

$$v = Hd, \tag{1.3}$$

where $H(a) \equiv \dfrac{\dot{a}}{a}$ is the Hubble parameter, which determines the rate of expansion and is defined in terms of the scale factor and it's time derivative, v is the velocity of an object's recession and d it's distance. Combining this equation with the Friedmann equation, which determines the rate of expansion based on the energy density of the constituents of the universe, gives

$$\frac{H^2(a)}{H_0^2} = \Omega_M a^{-3} + \Omega_R a^{-4} + \frac{\rho_{DE}(a)}{\rho_{\text{crit}}}, \tag{1.4}$$

Here $H_0 = H(a=1)$ is the Hubble Parameter today, Ω_M is the ratio of energy density of matter (dark matter and baryonic matter) today relative to the critical density of the universe ρ_{crit}, Ω_R the energy density of radiation today relative to the critical density, and $\rho_{DE}(a)$ is the energy density of DE as a function of scale factor, the form of which varies on the specific parameterization used for the equation of state $w(a)$. In the case where $w =$ constant, the DE term simplifies to $\rho_{DE}(a)/\rho_{\text{crit}} = \Omega_{DE} a^{-3(1+w)}$,

where Ω_{DE} is the fraction of the energy density of DE today to the critical density. Since the sum of the energy density fractions must equal 1 in a flat universe, we are able to substitute $\Omega_{DE} = 1 - \Omega_M - \Omega_R$, simplifying our analysis.

There are a few things one can take from Eq. 1.4. First, the relative energy density of radiation scales as a^{-4} meaning that as the universe grows, it decreases rapidly, to the point where in late times, radiation has a negligible effect on the expansion of the universe. This allows us to drop the radiation term whenever we calculate late-universe effects ($0 \lesssim z \lesssim 2$). In addition, since the energy density of radiation is very small compared to the matter energy density, Ω_R can be safely dropped from the Ω_{DE} substitution, leaving $\Omega_{DE} = 1 - \Omega_M$, further simplifying the analysis. However, for the early universe, radiation plays a critical role in determining the rate of the expansion, and a radiation term must be present for a correct calculation. The energy density of matter also decreases as the universe expands, but at a slower rate than radiation, resulting in matter always having a non-negligible effect on the expansion of the universe and thus should never be dropped.

The most interesting term, however, is the dark energy term. If we assume for this discussion that $w = -1$, then the energy density of DE remains a constant throughout the entire history of the universe. As radiation and matter densities continue to decrease while the universe expands, dark energy slowly plays a much more dominant role in the expansion, to the point where it is the dominant contributor in determining the future of the universe. In the far future, the effects of matter and radiation become negligible and DE dominates, resulting in exponential growth of the universe. However, in the early universe the DE contributions are negligible, meaning that any constraints on DE parameters are best done with late-universe effects.

The inverse of the Hubble parameter can be combined with the speed of light to give a distance, the Hubble distance $cH(z)^{-1}$. Integrating this distance over redshift (and setting $c = 1$) gives the total distance that light has traveled over that period.

This is the comoving distance

$$r(z) = \int_0^z \frac{dz'}{H(z')}, \tag{1.5}$$

where the initial redshift $z = 0$ corresponds to today. The comoving distance is the basic measure of distance in cosmology, with all the other types of distances being directly proportional to it. It is also the basis, along with the Hubble distance, for the basic unit of volume, the comoving volume.

1.2.2 The Growth Parameter and the Matter Power Spectrum

As mentioned earlier, dark energy also influences the formation of structure in the universe. There are several ways to quantify this; one way is by using the growth parameter $D(a) \equiv \delta(a)/\delta(0)$, where

$$\delta = \frac{\rho - \bar{\rho}}{\bar{\rho}} \tag{1.6}$$

is the perturbation away from the average energy density $\bar{\rho}$. This parameter provides us a measure of the amount of structure formation in the Universe; the larger the perturbations away from the mean are, the larger $\delta(a)$ (and thus $D(a)$) become, meaning more matter has collapsed into gravitationally bound objects resulting in more structure. The growth of structure, assuming general relativity, is governed by the differential equation

$$\ddot{\delta} + 2H\dot{\delta} - 4\pi G\rho_M\delta = 0, \tag{1.7}$$

where once again the dots are derivatives with respect to time, H is the Hubble parameter, ρ_M is the energy density of matter, and G is Newton's constant. A quick overview of this equation tells us a few things. First, the amount of structure in universe depends on the amount of matter as well as the strength of gravity. Second,

the expansion of the universe (seen here as the Hubble parameter) acts as a drag force against the rate of the growth of structure. The faster the rate of expansion, the less structure is formed, while a slower expansion rate necessarily allows for more growth of structure.

We can rewrite Eq. (1.7) as derivatives with respect to a (or, in this case, $\ln(a)$, the characteristic scale of e-folding). It is also useful to divide out the solution to a pure matter universe ($\delta \sim a$) by rewriting it in terms of the growth factor $g(a) = D(a)/a$ [53]. Making these changes, the differential equation becomes

$$g'' + \left[\frac{5}{2} - \frac{3}{2}w(a)\Omega_{DE}(a)\right] g' + \frac{3}{2}\left[1 - w(a)\right]\Omega_{DE}(a)g = 0, \tag{1.8}$$

where the primes denote derivatives with respect to $\ln(a)$, $w(a)$ is once again the equation of state of DE and (under the assumption that $w(a) = w$ is constant)

$$\Omega_{DE}(a) = \frac{(1-\Omega_M)a^{-3(1+w)}}{\Omega_M a^{-3} + (1-\Omega_M)a^{-3(1+w)} + \Omega_R a^{-4}}. \tag{1.9}$$

Another way to measure the amount of structure in the universe is by use of the linear matter power spectrum $P(k)$, which is the Fourier transform of the correlation of density perturbations $\xi(r_{12}) = \langle \delta_{\vec{r}_1} \delta_{\vec{r}_2} \rangle$. This quantity measures the amount of power as a function of scale; in other words, it measures the typical size of separation of structures in the universe and the size of those structures. A larger value of $P(k)$ for a wavenumber k (which is a measure of scale) means there's more power for that scale, and thus there is a higher chance of seeing large clumps of matter separated by that length scale. The power spectrum has the form

$$P(k,z) = P(k)D^2(z) = A\frac{4}{25}\frac{1}{\Omega_M^2}\left(\frac{k}{k_{\text{pivot}}}\right)^{n_s-1}\left(\frac{kc}{H_0}\right)^4 T^2(k)D^2(z), \tag{1.10}$$

where A and n_s are the amplitude (or normalization) of the power spectrum and the

spectral index respectively, k_{pivot} is the wavenumber at which n_s is computed, $D(z)$ is the growth parameter, and $T(k)$ is the matter transfer function. The transfer function quantifies the difference in growth for perturbations at different scales; perturbations that enter the horizon in the radiation dominated era do not grow until the universe beomes matter dominated. As a consequence, the power spectrum is initially constant, but then scales as $P(k) \propto k^{n_s-4}$ for wavenumbers greater than k_{equality}, the wavenumber of the mode that enters the horizon when radiation and matter densities are equal. This work makes use of the the Eisenstein and Hu matter transfer function for cold dark matter and neutrinos [24] which is faster to calculate compared to a more exact form calculated by codes such as `CAMB`. The differences in the results found in this work were compared and found to be very small between both codes.

1.3 Summary

In this chapter, I presented the observation of the acceleration of the expansion of the universe, and listed a few prominent explanations for this acceleration, the most widely accepted of these being dark energy. I discussed some of the effects the expansion has on properties of the universe, namely distances and growth of structure, and detailed some of the basic quantities used in cosmology to parameterize distances and the growth of structure.

The dark energy explanation to the expansion of the universe has many points to its favor, mainly in that it explains the expansion very well, though at the cost of a new form of energy that is not well understood. The simplest model, that of the cosmological constant (ΛCDM), describes DE as the vacuum energy of the universe. Even so, there are a variety of tests that can be done to better understand the properties of DE. The remainder of this work will focus on two of these tests: understanding how systematics affect the constraints on dark energy parameters and performing a consistency test of dark energy from its effects on geometry and growth.

CHAPTER 2

Probes of Dark Energy

2.1 Probing the Effects of Dark Energy

Ever since the discovery of the acceleration of the universe, there has been much work put into how we can measure the effects of that expansion, and in turn, of dark energy. Over the years since this discovery, many probes of dark energy have been proposed. Each of these probes measures various physical processes or effects in the universe that are theorized to be affected by dark energy [26, 84]. Because these different probes all measure different things, the various probes have different strengths and weaknesses. For example, Type Ia Supernovae are excellent probes of cosmological distance, but are rather poor at measuring the amount of structure formation in the universe. On the other hand, clusters of galaxies can be used to very effectively measure the growth of structure in the universe, though their sensitivity to cosmic distances is relatively minor. The combination of various probes allows us to place very powerful constraints on many cosmological parameters much more effectively than a single probe ever could. These tight constraints in turn can help us better understand the true nature of dark energy.

In this chapter, I will review various probes of dark energy, and explain the various strengths and weaknesses of each. In addition, I will go over how to calculate the theoretically expected values of these probes, which can then be compared to mea-

surements of those same values to place constraints on the cosmological parameters used to describe the models.

2.2 Type Ia Supernovae

The measurements of Type Ia supernovae (SNeIa) magnitudes have a long and storied history with DE; it was this probe that first gave us concrete evidence for DE [62, 65]. Since then, there has been an explosion of SNeIa data. One of the main advantages of SNeIa is that each individual supernova provides a distance measurement, as opposed to some of the other probes which require large numbers of galaxy or galaxy clusters to obtain a few data points. This, paired with the fact that supernova errors are small compared to some of these other probes, allow SNeIa to be a very powerful probe of DE. Their main downfall is that in order to get these small errors, the spectra of a potential SNeIa must be taken, which is a long and expensive process. In addition, SNeIa are subject to a large number of systematic uncertainties, and understanding these uncertainties, many which are dependent on the particular survey, is often a tedious process.

SNeIa are standardizable candles; their intrinsic magnitude varies predictably from one to another, allowing these variations to be easily corrected. Measuring a SNeIa's magnitude determines its distance. Along with its redshift measurement, this allows us to measure cosmological distances as a function of redshift.

A SN's theoretically expected magnitude is given by

$$m_{\rm th} = 5\log_{10}(H_0 D_L(z)) + \mathcal{M}, \tag{2.1}$$

where H_0 is the Hubble parameter today, $\mathcal{M}$ is a nuisance parameter that combines the absolute magnitude and the Hubble parameter[62] and is marginalized

analytically[18, 74] [1], and the luminosity distance is

$$D_L(z) = (1+z)r(z), \tag{2.2}$$

where $r(z)$ is the comoving distance. Because they only measure a cosmological distance, SNeIa are purely a geometric probe.

As previously mentioned, there are slight variations between SNeIa that can affect their intrinsic magnitude. Some SN take longer to reach peak brightness and fade. This broadening of a supernova's light curve is parameterized by a quantity known as the supernova's stretch s. Supernovae with broader light curves, and thus a higher stretch, tend to be brighter that those with a lower stretch. Likewise, the color $\mathcal{C}$ that the supernova exhibits also affects its intrinsic magnitude; bluer supernovae are brighter than their redder counterparts. To correct for these effects, the corrected magnitude is written as [29, 18, 68]

$$m_{\text{corr}} = m_B + \alpha_s(s-1) - \beta_{\mathcal{C}}\mathcal{C} \tag{2.3}$$

where m_B is the measured magnitude of the supernova, and where two new parameters, α_s and $\beta_{\mathcal{C}}$, the stretch and color nuisance parameters respectively, are introduced. These parameters allow variations in the amount of correction from these two effects, and must be marginalized for the final constraints of the cosmological parameters.

Because these distances all measured during the late universe epoch once DE becomes dominant, the effects of the radiation density on the magnitude are negligible. Thus, SNeIa only constrain two cosmological parameters, Ω_M and w, in addition to the nuisance parameters.

[1] There are actually two different values of $\mathcal{M}$ used in this work. A mass cut of the host-galaxy determines which $\mathcal{M}$ value applies for a specific supernova (here a mass cutoff value of $10^{10}M_\odot$ is used). This is meant to correct for properties of the host galaxy and is empirical in nature. These $\mathcal{M}$'s are both marginalized over analytically when the likelihood is computed. For more details see the end of section 3.3.1. Mention of the second $\mathcal{M}$ parameter is suppressed for simplicity.

2.3 Cosmic Microwave Background

The hot and cold spots of the cosmic microwave background (CMB) anisotropies provide an excellent standard ruler: their angular separation, combined with the sound horizon distance that is independently well-determined, provide a single yet accurate measurement of the angular diameter distance

$$D_A(z_*) = \frac{1}{1+z_*} r(z_*), \tag{2.4}$$

where z_* is the redshift of recombination. In addition to being very high-redshift, this measurement of $D_A(z_*)$ is different from the low-redshift measurements in that the physical matter density $\Omega_M h^2$ is essentially fixed by the CMB peaks' height. This is why the CMB peaks location measurement curves in a very complementary degeneracy direction in the Ω_M–w plane to low-redshift measurements of distance[27].

For simplicity and clarity, only the geometrical measurement provided by the CMB acoustic peaks' locations is used for this work. The integrated Sachs-Wolfe (ISW) effect of dark energy which imprints on the CMB angular power spectrum on very large scales adds very little to the information due to large cosmic variance. The CMB is also sensitive to the physics at the last-scattering surface [88], but the late universe is what is mostly of interest, when dark energy becomes significant. Therefore, the aforementioned angular diameter distance to last scattering with $\Omega_M h^2$ fixed is used, referred to as the "shift parameter" R and defined as

$$R = \sqrt{\Omega_m H_0^2}\,(1+z_\star) D_A(z_\star). \tag{2.5}$$

Since R is essentially the angular diameter distance to the last scattering surface with $\Omega_M h^2$ fixed [27], it is only sensitive to two parameters: Ω_M and w.

2.4 Baryon Acoustic Oscillations

Baryon acoustic oscillations (BAO) are features that arise from the propagation of sound waves in the early universe. The distance the sound wave can travel between the Big Bang and the present – the sound horizon – imprints a characteristic scale not only in the CMB fluctuations, but also in the clustering two-point correlation function of galaxies. Roughly speaking, the two-point correlation function is enhanced by $\sim 10\%$ at distances of $\sim 10 H_0^{-1}$Mpc. This latter distance is, similar to the CMB case, well-measured by early-universe parameters ($\Omega_M h^2$ and $\Omega_B h^2$ principally), but its observation is dependent on the expansion history of the universe between the time that light from the galaxies is emitted and today.

Specifically, for two galaxies at the same redshift separated by comoving distance r and seen with separation θ, we have $\theta = r/D_A(z)$ which enables measurement of the angular diameter distance given a known separation between galaxies. Similarly, two galaxies at the same angular location separated by redshift difference Δz are separated by comoving distance r, with the two quantities related via $\Delta z = rH(z)$. The information from these transverse and radial sensitivities for a sample of galaxies can be conveniently combined into a single quantity, a generalized distance $D_V(z_{\rm eff})$ [23] of the form

$$D_V(z) = \left(\frac{(1+z)^2 D_A^2(z) cz}{H(z)} \right)^{1/3}. \tag{2.6}$$

This can then be compared to the size of the comoving sound horizon $r_s(z_d)$ at the redshift of the baryon drag epoch (the redshift at which baryons are released from the Compton drag of photons after they've been decoupled)

$$r_s(z) = \frac{1}{\sqrt{3}} \int_0^{1/(1+z)} \frac{da'}{a'^2 H(a') \sqrt{1 + 3\rho_B/4\rho_R}}. \tag{2.7}$$

BAO surveys measure the ratio $r_s(z_d)/D_V(z_{\rm eff})$ (or its inverse), effectively measuring

how much the characteristic size of the separation of objects has changed over time.

It is important to note that a radiation term must be included in $H(a)$ in Eq. (2.7). A useful relation for this is $\Omega_R = \Omega_M a_{\rm eq}$, where $a_{\rm eq} = 1/(1+z_{\rm eq})$ is the scale factor at matter-radiation equality and

$$z_{\rm eq} \approx 25000\ \Omega_M h^2 \left(\frac{T_{\rm CMB}}{2.7{\rm K}}\right)^{-4}. \tag{2.8}$$

The ratio of the baryonic density to the radiation density can be approximated as

$$\frac{3\rho_b}{4\rho_\gamma} \approx 31500\ \Omega_B h^2 \left(\frac{T_{\rm CMB}}{2.7{\rm K}}\right)^{-4} a. \tag{2.9}$$

A value of $T_{\rm CMB} = 2.7255$K is used in this work.

The redshift of the drag epoch can be approximated by the fitting function[24]

$$z_d = \frac{1291(\Omega_M h^2)^{0.251}}{1+0.659(\Omega_M h^2)^{0.828}} \left[1 + b_1 (\Omega_B h^2)^{b_2}\right], \tag{2.10}$$

where

$$b_1 = 0.313(\Omega_M h^2)^{-0.419} \left[1 + 0.607(\Omega_M h^2)^{0.674}\right] \tag{2.11}$$

$$b_2 = 0.238(\Omega_M h^2)^{0.223}. \tag{2.12}$$

Some surveys provide a different measured quantity, the acoustic parameter $A(z)$, defined as

$$A(z) = \frac{\sqrt{\Omega_M H_0^2} D_V(z)}{z}. \tag{2.13}$$

This quantity provides similar information as $D_V(z)$, but is usually not combined with the sound horizon, and allows for tests involving a geometric-only quantity, without having to depend on early universe physics.

2.5 Cluster Counts and Mean Masses

The number of galaxies in a galaxy cluster, or cluster count, provides an excelent measurement of both growth of stucture and expansion history [4]. The number density of galaxies within the cluster is a proxy to the mass of the cluster, providing a measure of the growth of structure of the universe. Cluster counts also provide a measure of the geometric properties of the universe, since the number of galaxies in a cluster also depends on the volume of space they take up, a geometric property. The product of the number density and the volume gives the number of galaxy clusters in a mass and redshift range, which we can use to compare to cluster count measurements.

Deriving the number of galaxy clusters within a mass and redshift range is fairly straightforward: we begin with the aforementioned product

$$N = nV, \tag{2.14}$$

where n is the number density and V the volume. We can expand both of these terms to include a range of masses and redshifts

$$N = \int dM\ dz\ \frac{dn}{dM}\ \frac{dV}{dz}\ \psi(M)\ \phi(z), \tag{2.15}$$

where dV/dz is the comoving volume per redshift, dn/dM is the halo mass function, and $\psi(M)$ and $\phi(z)$ are top-hat binning functions that determine the mass and redshift range of a particular bin, respectively. In other words, $\psi(M) = 1$ if M is in a defined redshift bin and 0 otherwise; likewise for $\phi(z)$.

A cluster's mass and redshift are not directly observable; instead, we rely on the cluster mass-richness relation and the photometric redshift of the member galaxies. With this in mind, we can define $P(N_{200}|M)$ to be the probability that a cluster of mass M has a richness N_{200}. Here richness refers to the number of galaxies within a

galaxy cluster, and the boundary of the cluster is defined to be a sphere of a radius such that the average matter density within the sphere is 200 times that of the mean density of matter (i.e. for an overdensity $\Delta = 200$). Likewise, we define $P(z_{\rm photo}|z)$ to be the probability that a cluster at a true redshift z is measured to have a photometric redshift of $z_{\rm photo}$. Redefining $\psi = \psi(N_{200})$ and $\phi = \phi(z_{\rm photo})$, the expected number of clusters becomes

$$\langle N \rangle = \int dM \; dz \; \frac{dn}{dM} \; \frac{dV}{dz} \; \langle \psi | M \rangle \; \langle \phi | z \rangle, \tag{2.16}$$

which introduces the probability weighting functions

$$\langle \psi | M \rangle = \int dN_{200} \, P(N_{200}|M) \psi(N_{200}), \tag{2.17}$$

$$\langle \phi | z \rangle = \int dz_{\rm photo} \, P(z_{\rm photo}|z) \phi(z_{\rm photo}). \tag{2.18}$$

Here $P(z_{\rm photo}|z)$ is modeled as a Gaussian distribution as discussed in Reference [66]. Meanwhile, $P(N_{200}|M)$ is modeled as log-normal distribution, primarily because $\ln N_{200}$ is expected to vary as a function of $\log M$, so that $\ln N_{200}$ rather than N_{200} is treated as the main parameter. The variation of $\ln N_{200}$ with $\log_M$ is assumed in this work to be linear, resulting in two free parameters. The variance of the distribution is also unknown, and is also thus treated as free parameter. These parameters are marginalized over in the analysis. More details about these functions will be provided later.

In a similar fashion, we can define the expected total cluster mass for a given richness and photometric redshift bin as

$$\langle N \bar{M} \rangle = \beta \int dM \; dz \; M \frac{dn}{dM} \; \frac{dV}{dz} \; \langle \psi | M \rangle \; \langle \phi | z \rangle, \tag{2.19}$$

where the nuisance parameter β is introduced to take into account the uncertainty in the calibration of mass.

The comoving volume is simply

$$\frac{dV}{dz} = \Omega_{\rm sky} \frac{c\ (1+z)^2 D_A^2(z)}{H(z)} \tag{2.20}$$

where there are two powers of the angular distance for the angular distances and one power of the Hubble distance $cH^{-1}(z)$ for the radial distance. $\Omega_{\rm sky}$ is the solid angle covered by the survey making the measurements.

For this work, the halo mass function used is the Tinker Mass Function [80]

$$\frac{dn}{dM} = f(\sigma, z) \frac{\bar{\rho}_M}{M} \frac{d \ln \sigma^{-1}}{dM} \tag{2.21}$$

where $\bar{\rho}_M = \Omega_M \bar{\rho}_{\rm crit}$ is the energy density of matter, and $f(\sigma, z)$ is a fitting function

$$f(\sigma, z) = A(z) \left[\left(\frac{\sigma}{b(z)} \right)^{-a(z)} + 1 \right] e^{-c_0/\sigma^2}. \tag{2.22}$$

The redshift-dependent functions are defined as

$$A(z) = A_0 (1+z)^{-0.14} \tag{2.23}$$

$$a(z) = a_0 (1+z)^{-0.06} \tag{2.24}$$

$$b(z) = b_0 (1+z)^{-\alpha(\Delta)} \tag{2.25}$$

$$\log_{10} \alpha(\Delta) = - \left(\frac{0.75}{\log_{10}(\Delta/75)} \right)^{1.2} \tag{2.26}$$

and the coefficients $\{A_0, a_0, b_0, c_0\} = \{0.186, 1.47, 2.57, 1.19\}$ for an overdensity $\Delta = 200$ [80].

The amplitude of matter fluctuations σ is defined as

$$\sigma^2(R, z) = \int P(k, z) \hat{W}^2(kR) d \ln k \tag{2.27}$$

where $\hat{W}$ is a the Fourier transform of the real-space top hat window function

$$\hat{W}(x) = 3\sin(x) - \frac{x\cos(x)}{x^3} \tag{2.28}$$

and $P(k, z)$ is the linear matter power spectrum as defined in Eq. 1.10. The radius R in Eq. 2.27 is a function of mass

$$R(M) = \left(\frac{3M}{4\pi\bar{\rho}_M}\right)^{1/3} \tag{2.29}$$

Eq. 2.27 also allows for the definition of the parameter $\sigma_8 = \sigma(R = 8h^{-1}\text{Mpc}, z = 0)$, which for this work is considered a derived parameter.

As stated earlier, $P(z_{\text{photo}}|z)$ is modeled as a Gaussian distribution [66]. In any survey, an object located at a true redshift z is expected to be measured at a photometric redshift equal to the true redshift, or $\langle z_{\text{photo}}|z\rangle = z$. Thus, the functional form for this distribution is

$$P(z_{\text{photo}}|z) = \frac{1}{\sqrt{2\pi\sigma_z^2}} e^{-\frac{(z_{\text{photo}} - z)^2}{2\sigma_z^2}}. \tag{2.30}$$

The value of the variance σ_z^2 depends on the specific survey used (Reference [66] uses $\sigma_z = 0.08$).

In contrast, the probability of a certain richness given a mass $P(N_{200}|M)$ is a log-normal distribution

$$P(N_{200}|M) = \frac{1}{N_{200}\ \sqrt{2\pi\sigma_{NM}^2}}\ e^{-\frac{(\ln N_{200} - \langle \ln N_{200}|M\rangle)^2}{2\sigma_{NM}^2}}. \tag{2.31}$$

The expected value for the richness of a cluster given a mass is assumed to vary

linearly with $\log_{10} M$

$$\langle \ln N_{200}|M\rangle = \left(\frac{\langle \ln N_{200}|M_2\rangle - \langle \ln N_{200}|M_1\rangle}{\log_{10} M_2 - \log_{10} M_1}\right)\log_{10} M + \frac{\log_{10} M_2\langle \ln N_{200}|M_1\rangle - \log_{10} M_1\langle \ln N_{200}|M_2\rangle}{\log_{10} M_2 - \log_{10} M_1}, \tag{2.32}$$

which simplifies to

$$\langle \ln N_{200}|M\rangle = \frac{\log_{10}(M/M_1)\langle \ln N_{200}|M_2\rangle - \log_{10}(M/M_2)\langle \ln N_{200}|M_1\rangle}{\log_{10}(M_2/M_1)} \tag{2.33}$$

Here M_1 and M_2 are masses defined during the analysis, which for this work are set to $M_1 = 1.3 \times 10^{14} M_\odot$ and $M_2 = 1.3 \times 10^{15} M_\odot$. $\langle \ln N_{200}|M_1\rangle$ and $\langle \ln N_{200}|M_2\rangle$ are considered nuisance parameters, and are marginalized over during the analysis of the cluster data. The parameter $\sigma^2_{NM} = \mathrm{Var}(\ln N_{200}|M)$ in Eq. 2.31 is also considered a nuisance parameter and marginalized during analysis.

2.6 Weak Lensing

Weak gravitational lensing, or weak lensing (WL), by the large-scale structure is another powerful probe of the growth of structure in the universe. WL surveys measure the shear of galaxies, that is, the amount a galaxy image is "stretched" due to the lensing mass in front. The amount of shear also depends on the position of both the object being lensed and the object doing the lensing. As such, WL is also sensitive to geometric properties of the universe along the line of sight. Thus, WL is a great way to measure both the geometric and growth effects of dark energy. By calculating the two-point correlation function of these shears across the sky, we can extract useful information about the both the large-scale structure and the expansion history of the universe[2].

[2]Many thanks to Dragan Huterer for writing the code used to analyze the two-point shear correlation function for WL.

The two-point correlation function of galaxy shear is given by [31]

$$\chi_{\pm}^{ij} = \frac{1}{2\pi} \int_0^{\infty} dl \; l \; P_{\kappa}^{ij}(l) \; J_{\pm}(l\theta) \tag{2.34}$$

where l is the multipole, $J_+(x) \equiv J_0(x)$ and $J_-(x) \equiv J_4(x)$ are the zeroth and fourth order Bessel functions of the first kind, respectively, and i and j refer to the ith and jth tomographic bin, respectively. In the Limber approximation, which only takes into account modes perpendicular to the line of sight and is an excellent approximation at scales of interest, the weak lensing convergence power spectrum at angular wave number l is defined as

$$P_{\kappa}^{ij}(l) = \int dz \frac{r^2(z)}{H(z)} \; W_i(z) W_j(z) P\left(k = \frac{l}{r(z)}\right), \tag{2.35}$$

where $r(z)$ and $H(z)$ are the comoving distance and Hubble parameter, respectively, $P(k)$ is the power spectrum, and the weight function $W_i(z)$ is

$$W_i(z) = \frac{3}{2} \Omega_M H_0^2 \; q_i(z)(1+z). \tag{2.36}$$

Here, the function $q_i(z)$ is the lensing efficiency, given by

$$q_i(z) = r(z) \int_z^{\infty} \frac{dz'}{H(z')} \; n_i(z') \frac{r(z') - r(z)}{r(z')}, \tag{2.37}$$

where $n_i(z)$ is the distribution of the lensed galaxies in each redshift bin, normalized to $\int n_i(z')dz' = 1$, and is provided by the survey taking measurements.

Special attention is required when modeling the power spectrum due to the small angles that WL surveys probe, where we see strongly non-linear scale clustering [40]. To correctly take these effects into account, the updated `halofit` [78] prescription for non-linear clustering is used.

2.7 Redshift Space Distortions

Redshift space distortions (RSD) refer to the effect of how massive dark matter halos affect the velocity distribution of galaxies within them and nearby. The galaxies' radial velocities contribute to their measured redshift in a survey. Since galaxies behind a halo tend to be moving towards the observer, their apparent redshift is lowered by their peculiar velocity, resulting in an overall lower measured redshift. A similar but opposite effect occurs for galaxies in front of the halo as they move away from the observer. This change in redshift leads to an apparent compression of clustering in the radial direction compared to the transverse directions, which does not experience this effect. On smaller scales, the random directions of the galaxies' peculiar velocities leads to a measurement of the so-called "Fingers of God" effect [44], boosting the radial signal. Measuring this effect at different redshifts allows us to place constraints on the growth of structure across cosmic history.

RSD measurements are particularly sensitive to the cosmological parameter combination $f(a)\sigma_8(a)$, commonly written as $f\sigma_8$. $\sigma_8(a)$ is the amplitude of matter fluctuations at $8h^{-1}$Mpc, as defined earlier (though now at an arbitrary value of the scale factor), and

$$f(a) = \frac{d\ln D}{d\ln a}, \tag{2.38}$$

where $D(a)$ is once again the growth paramter.

RSD measurements are also affected by the Alcock-Paczynski effect. When calculating the correlation function which eventually lead to values of $f\sigma_8$, a fiducial cosmology is typically assumed to calculate the separation between galaxies in the radial and transverse directions. Any differences in the assumed cosmology and the cosmology of a test model results in a difference in the clustering of galaxies along the line of sight compared to the transverse directions, or anisotropic clustering. To account for this effect, the measurements the Hubble parameter $H(z)$ for the radial

direction and the angular distance $D_A(z)$ for the transverse direction are included in the analysis either by the Alcock-Paczynski effect parameter

$$F(z) = (1+z)H(z)D_A(z)/c, \tag{2.39}$$

or by including $H(z)$ and $D_A(z)$ directly. Since these are distance measurements, the Alcock-Paczynski effect allows RSD to probe geometry as well as growth.

2.8 Summary

In this chapter, I gave a brief overview of the probes used in subsequent chapters: type Ia Supernovae, the cosmic microwave background shift parameter, baryon acoustic oscillations, galaxy cluster counts, weak lensing shear two-point correlations, and redshift space distortions. In addition, I explained whether the probes are sensitive to the geometric properties of the universe, the growth of structure formation, or both. I also presented the methods used to calculate the theoretically expectated values and other quantities when given a set of cosmological parameters.

By measuring different effects, each of these probes provides a unique insight into the workings of DE. As we will se in the subsequent chapters, by themselves, each probe produces fairly weak constraints, given that certain probes are subject to various degeneracies in cosmological parameters. However, when combined, the various probes break degeneracies and complement each other very well. For this reason, much effort has gone into using various probes to provide different measurements, as well as coming up with new probes that can break degeneracies and provide tighter constraints. By combining these various constraints our knowledge of DE becomes much stronger and brings us closer to understanding its properties and nature.

CHAPTER 3

The Effects of SNe Systematics on DE Principal Components

3.1 Introduction to Supernova Systematics

In this chapter, I study the effects of Type Ia Supernovae systematics on dark energy parameter constraints by including the covariance between SNeIa measurements. This covariance, which primarily consists of systematic effects, have been quantified in detail by Reference [18], and its inclusion weakens the constraints on dark energy parameters for simple parameterizations on the dark energy equation of state. I study the effects of the systematics on a general model of DE described by the principal components of the equation of state, though I first review the effects on simpler models. The supernova data is combined with BAO and CMB data to break degeneracies.

Many papers have studied the effects of systematics [86, 32, 47, 18], but they typically limit their analysis to a constant equation of state w, or at the very least have included the additional parameter w_a to describe a simple scale-variation of the equation of state. My goal here is to test the effects on as general a model of DE as possible, using a description of ten or so parameters. The work here is complementary to work done by References [59, 57] (see also [38, 83, 94, 92, 34, 43, 75, 72, 90]), which studied constraints on general descriptions of DE using current data, but without

studying the effects of systematics. Work done in this Chapter first appeared in Reference [68].

3.2 Generalizing the Dark Energy Equation of State

The assumption that the dark energy equation of state w is constant throughout time is a reasonable one for most purposes. Indeed, the most commonly accepted model, ΛCDM, is described by a constant equation of state $w = -1$. However, it is important to test even the most basic assumptions, and a very straightforward way to do this is by allowing the equation of state to vary as a function of scale factor, i.e. $w = w(a)$. In fact, several dark energy theories predict a variation in the value of w due to, for example, scalar field properties such as those found in quintessence models. Thus, allowing a scale-varying equation of state provides an avenue that allows us to potentially rule out ΛCDM in favor of competing theories.

More general models allow of more flexibility in the properties of DE we can test. However, due to a larger number of parameters needed to fully define the model, the ability to constrain it given a particular set of data is lower than a comparable simpler model. Finding a useful parameterization for $w(a)$ has been the subject of many papers, and there have been some formulations that stand above the rest. In the following subsections, I will detail some of the generalized parameterizations that have been proposed for testing DE properties.

3.2.1 w_0 and w_a Parameterization of the Equation of State

Parameterizing the equation of state with only one parameter prevents us from knowing if its value has varied throughout the history of the universe. We can generalize

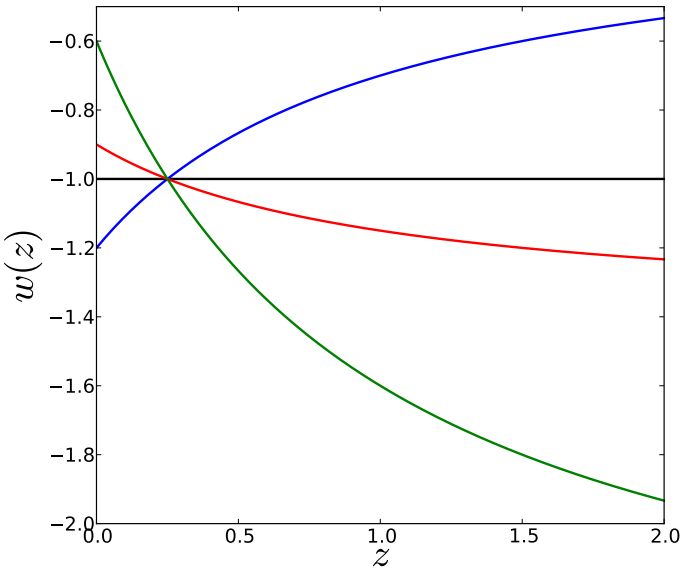

Figure 3.1: Plot showing several functions of $w(z)$ for various values of w_0 and w_a. The functions are: $(w_0, w_a) = (-1, 0)$ (Black), $= (-1.2, 1)$ (Blue), $= (-0.9, -0.5)$ (Red), $= (-0.6, -2)$ (Green). All of these model are found within the 68.3% contour after constraints have been obtained (see Fig. 3.7). Note that all of the functions intersect around $z = 0.2 - 0.3$. This area is where most of the information from the data is found and so provides the best constraining power for the value of $w(z)$, a detail which is also apparent with the principal component parameterization.

the equation of state slightly by introducing a scale dependence of the form [52, 15]

$$\begin{aligned} w(a) &= w_0 + w_a(1-a) \\ &= w_0 + w_a\left(\frac{z}{1+z}\right) \end{aligned} \tag{3.1}$$

where a is the scale factor and z is the redshift as described in Chapter 1, and w_0 and w_a are cosmological parameters which describe the evolution of the equation of state and will be constrained using cosmological data from surveys. In the ΛCDM model, $w_0 = -1$ and $w_a = 0$. Several other functions using this parameterization are shown in Fig. 3.1. The dark energy term from Eq. 1.4 takes on the form

$$\frac{\rho_{DE}(z)}{\rho_{\text{crit}}} = \Omega_{DE}(1+z)^{3(1+w_0+w_a)}e^{-3w_a z/(1+z)} \tag{3.2}$$

There are several advantages to using this parameterization for the equation of state. First, it allows us to test the scale-dependence (and thus time-dependence) of the equation of state. It also reduces to the regular constant w for low redshifts, but is still well behaved at high redshifts. Additionally, it is fairly accurate in reconstructing many of the scalar field predictions for the equation of state, allowing for the testing of quintessence models. And of course, it is still simple enough to be manageable.

3.2.2 Principal Components of the Equation of State

Principal components (PC) are a statistical tool that can be utilized to parameterize the equation of state more generally. This allows for a detailed study of the variation of the equation of state as a function of scale factor. The PCs form a complete set of orthonormal basis vectors which combine linearly and give a very general parameterization for $w(z)$. Additionally, these PCs are ordered by increasing variance, so that the first PCs would be constrained the most by the observational data. As such, only the first few PCs from a total set are needed when placing constraints.

The PCs are precomputed using a Fisher matrix centered around a ΛCDM model with $\Omega_M = 0.25$ [59], and the first 10 PCs are shown in Fig. 3.2; for more details on the PC calculation, see Appendix A. The PCs combine linearly to form $w(a)$, which has the form [58]

$$w(a) = -1 + \sum_{i=0}^{N-1} \alpha_i e_i(a). \tag{3.3}$$

Here $e_i(a)$ are the PCs, N is the total number of PCs used in a particular analysis, and α_i are the PC amplitudes whose values are constrained using data from surveys. For the ΛCDM model, all $\alpha_i = 0$; these adopted as the fiducial values. The PCs are then analyzed, along with the rest of the cosmological parameters and nuisance parameters, to place constraints. In this work, only the first 10 PC amplitudes are constrained; most of the data are not powerful enough or of high enough redshift to

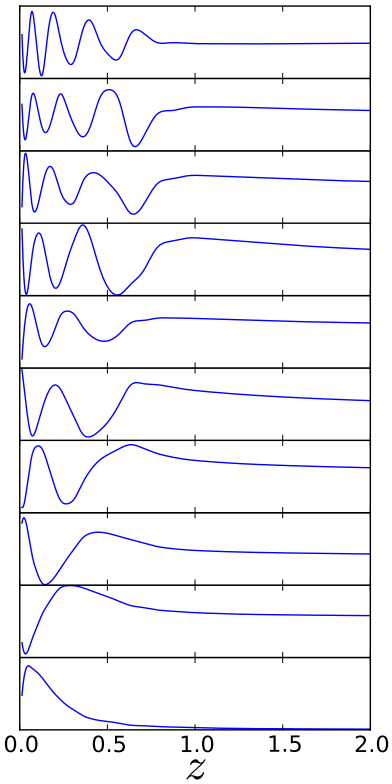

Figure 3.2: Plot of the first ten PCs in order (from bottom to top) of increasing variance. The PCs were obtained using ΛCDM values, but with errors from real data; see Appendix A for details. The PCs show us that most of the constraining power of the data is found around $z = 0.2 - 0.3$, similar to what was determined in the $w_0 - w_a$ plot in Fig. 3.1.

constrain the rest of the amplitudes very well. These are kept at the fiducial values during the analysis.

3.3 Data Sources

The main goal of this analysis is to test the effects of Type Ia supernova systematics on constraints of the equation of state. This requires mainly testing the geometrical properties of dark energy; thus, only cosmological probes that primarily test geometric properties of DE are included for this analysis. The data sources included are the SNeIa magnitude measurements from the Supernova Legacy Survey (SNLS), a combination of BAO data from a variety of surveys, and a measurement of the CMB

shift parameter from the 7-year data release of the Wilkinson Microwave Anisotropy Probe (WMAP7).

3.3.1 Supernova Legacy Survey

The Supernova Legacy Survey (SNLS) [18] has compiled a sample of 472 supernova magnitude and redshift measurements from a variety of surveys, which include the Sloan Digital Sky Survey (SDSS), several high-redshift SNeIa observed by the Hubble Space Telescope (HST), low-redshift SNeIa data points from various ground-based telescopes (Low-z), and SNLS itself. These data points are illustrated in a Hubble diagram in Fig. 3.3 and summarized in Table 3.1.

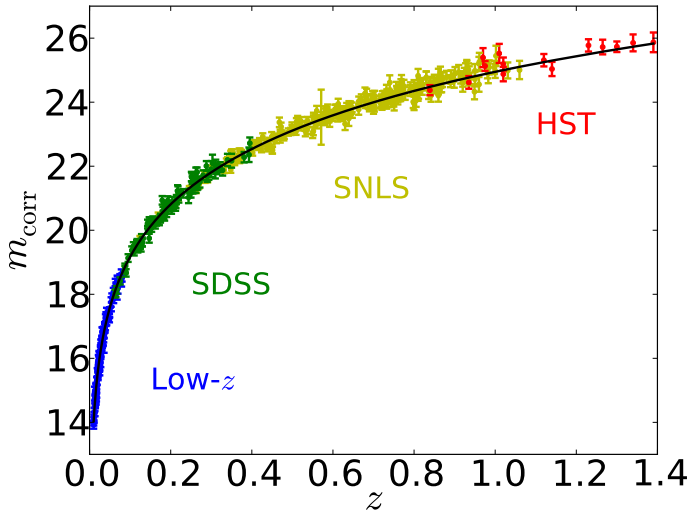

Figure 3.3: Plot showing a Hubble diagram of the 472 supernovae used in this work. The error bars are from diagonal-only statistical errors. The black line shows a well-fitting ΛCDM model.

Included within the SNLS dataset are the statistical errors for each supernova. These errors form a diagonal covariance matrix of the form [18, 68]

$$D_{ii}^{\rm stat} = \sigma_{m,i}^2 + \alpha_s^2\sigma_{s,i}^2 + \beta_{\mathcal{C}}^2\sigma_{\mathcal{C},i}^2 + \sigma_{\rm int}^2 + \left(\frac{5(1+z_i)}{z_i(1+z_i/2)\ln 10}\right)^2 \sigma_{z,i}^2 + \sigma_{\rm lensing}^2 + \sigma_{\text{host correction}}^2 + D_{ii}^{ms\mathcal{C}}(\alpha_s, \beta_{\mathcal{C}}). \quad (3.4)$$

Source	$N_{\rm SN}$	Redshift range	$\sigma_{\rm int}$
Low-z	123	$0.01 - 0.1$	0.1133
SDSS	93	$0.06 - 0.4$	0.0989
SNLS	242	$0.08 - 1.05$	0.0675
HST	14	$0.7 - 1.4$	0.0815

Table 3.1: Summary of SN Ia observations included in the SDSS catalog, showing the number of SNe included from each survey and the approximate redshift ranges. Also included are the intrinsic scatters of each survey, denoted $\sigma_{\rm int}$.

Here, $\sigma_{m,i}$, $\sigma_{s,i}$, $\sigma_{\mathcal{C},i}$, and $\sigma_{z,i}$ are the statistical uncertainties for the measured magnitude, stretch, color, and redshift, respectively, of the ith supernova. The z term translates the error in redshift into an error in magnitude. To correctly account for the intrinsic scatter of SNeIa within each survey, the term $\sigma_{\rm int}$ is included, with a different value associated with each of the four surveys (see Table 3.1 for these values). Also included are terms for the uncertainty due to gravitational lensing and galaxy host mass corrections.

The term $D_{ii}^{ms\mathcal{C}}$ represents a combination of the covariance terms for magnitude, stretch, and color for the ith supernova

$$D_{ii}^{ms\mathcal{C}}(\alpha_s, \beta_\mathcal{C}) = 2\alpha_s D_{ii}^{ms} - 2\beta_\mathcal{C} D_{ii}^{m\mathcal{C}} - 2\alpha_s\beta_\mathcal{C} D_{ii}^{s\mathcal{C}}. \tag{3.5}$$

It is important to note that the statistical portion of the total covariance matrix is a function of the stretch and color nuisance parameters α_s and $\beta_\mathcal{C}$, and must be calculated each time the value of these parameters change.

The SNLS team has also provided a 472×472 systematic error covariance matrix, which takes into account systematics from various sources, including Malmquist Bias, systematic effects due to Milky Way dust, and calibration errors in the survey instruments, among others. A full list of these systematic errors can be found in Reference [18]. A similar equation to Eq. (3.4) can be used for these off-diagonal systematic portions of the total uncertainty, where different values must be combined with the

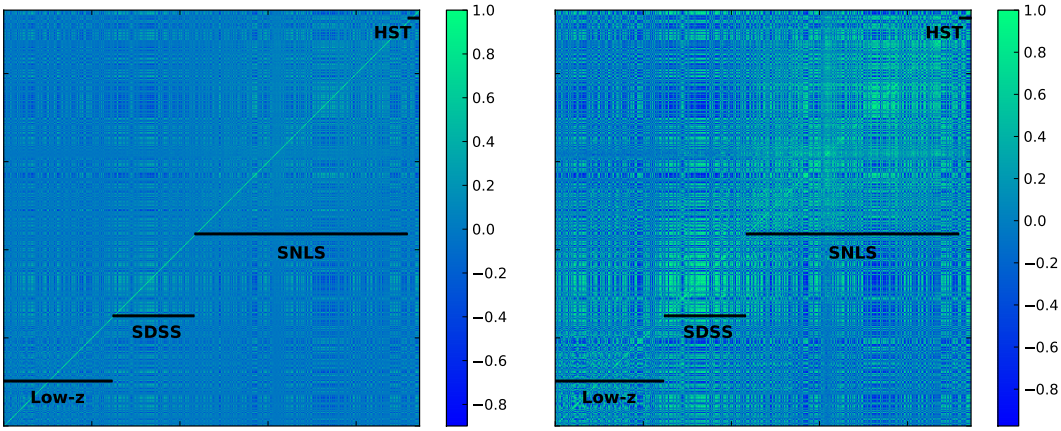

Figure 3.4: Left panel: correlation matrix obtained from the complete covariance matrix $\mathbf{C}^{\rm full}$, sorted first by survey and then by redshift within each survey. Right panel: the same as the left, but using only the systematic covariance matrix $\mathbf{C}^{\rm sys}$. Both cases assume $\alpha_s = 1.43$ and $\beta_c = 3.26$, the best-fit values for the flat $w = \text{const}$ model.

α_s and $\beta_{\mathcal{C}}$ parameters. The elements of systematic covariance matrix (see Reference [18] for details) are calculated using

$$C_{ij}^{\rm sys} = \sum_{k=1}^{K} \left(\frac{\partial m_{{\rm corr},i}}{\partial S_k} \right) \left(\frac{\partial m_{{\rm corr},j}}{\partial S_k} \right) (\Delta S_k)^2, \tag{3.6}$$

where the sum is over k systematics S_k, ΔS_k is the size of the systematic, and $m_{\rm corr} = m_{\rm corr}(\mathbf{p})$ is the theoretical prediction for the magnitude from the set of cosmological parameters $\mathbf{p}$ defined in Eq. (2.3). The full covariance is then given by

$$\mathbf{C}^{\rm full} = \mathbf{D}^{\rm stat} + \mathbf{C}^{\rm sys}. \tag{3.7}$$

A plot of the covariance matrix (at the best-fit values $\alpha_s = 1.43$ and $\beta_{\mathcal{C}} = 3.26$) is shown in Fig. 3.4.

The full covariance matrix, along with the magnitude data from SNLS, allows us to construct the χ^2 statistic. Due to the use of two values of $\mathcal{M}$, the analytic

marginalization of these values results in

$$\chi^2_{\rm SNe} = a + \ln\frac{e}{2\pi} + \ln\frac{g}{2\pi e} - \frac{b^2 f}{g} - \frac{c^2 e}{g} + 2\frac{bcd}{g}, \tag{3.8}$$

where

$$\begin{aligned} a &= \Delta\mathbf{m}^T \mathbf{C}^{-1}_{\rm full} \Delta\mathbf{m} \\ b &= \Delta\mathbf{m}^T \mathbf{C}^{-1}_{\rm full} \mathbf{K}_1 \\ c &= \Delta\mathbf{m}^T \mathbf{C}^{-1}_{\rm full} \mathbf{K}_2 \\ d &= \mathbf{K}_1^T \mathbf{C}^{-1}_{\rm full} \mathbf{K}_2 \\ e &= \mathbf{K}_1^T \mathbf{C}^{-1}_{\rm full} \mathbf{K}_1 \\ f &= \mathbf{K}_2^T \mathbf{C}^{-1}_{\rm full} \mathbf{K}_2 \\ g &= ef - d^2. \end{aligned}$$

Here, $\Delta\mathbf{m} = \mathbf{m}_{\rm corr} - \mathbf{m}_{\rm th}(z) + \mathcal{M}$, where $\mathbf{m}_{\rm corr}$ is the corrected observed magnitude as defined in Eq. 2.3. The two vectors $\mathbf{K}_1$ and $\mathbf{K}_2$ describe whether a certain supernova's host galaxy's mass is below or above the cutoff of $M = 10^{10} M_\odot$, which determines which value of $\mathcal{M}$ is assigned to the supernova's magnitude. If a supernova's host galaxy is in the first set, its corresponding location in $\mathbf{K}_1$ is 1; otherwise it is 0. The same but opposite thing occurs for $\mathbf{K}_2$. Note here that $\Delta\mathbf{m}$ is independent of $\mathcal{M}$.

3.3.2 BAO Surveys and WMAP7

For this work, a collection of measurements of the acoustic parameter $A(z)$ from various surveys is used, mainly due to its dependence on the geometrical effects of DE rather than its growth effects, which are not of interest for this analysis. The measurements include data from the Six-degree Field Galaxy Survey (6dFGS) [8], the Sloan Digital Sky Survey Data Release 7 (SDSS DR7) [61], the WiggleZ survey

Sample	z_{eff}	$A(z_{\text{eff}})$
6dFGS	0.106	0.526 ± 0.028
SDSS DR7	0.20	0.488 ± 0.016
SDSS DR7	0.35	0.484 ± 0.016
WiggleZ	0.44	0.474 ± 0.034
BOSS	0.57	0.444 ± 0.014
WiggleZ	0.60	0.442 ± 0.020
WiggleZ	0.73	0.424 ± 0.021

Table 3.2: Summary of measurements of BAO acoustic parameter $A(z)$. The table lists the survey from which the measurement comes, the effective redshift of the survey (or its subsample), and the measured value $A(z)$.

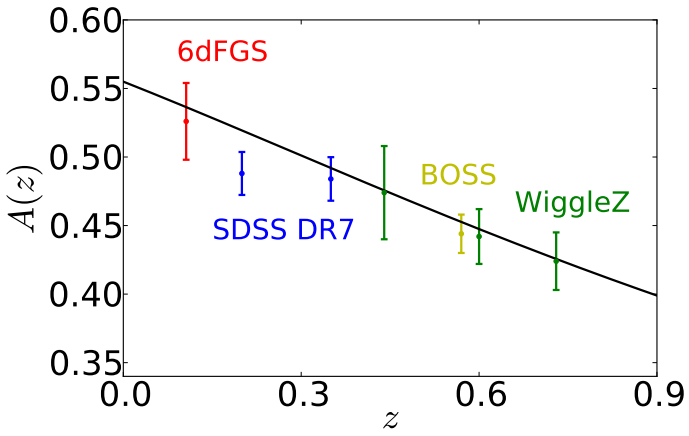

Figure 3.5: Plot showing the measurements of the BAO Acoustic parameter $A(z)$ along with their associated diagonal errors. The various data points are color coded according to the survey they come from. The black line shows the same ΛCDM model as seen in Fig. 3.3.

[12, 13], and the SDSS Baryon Oscillation Spectroscopic Survey (BOSS) [70, 5] and is summarized in Table 3.2 and plotted in Fig. 3.5. It is important to note that the SDSS points are correlated with a correlation coefficient of 0.337, while the WiggleZ points are correlated with the coefficient 0.369 for the pair $z = (0.44, 0.6)$ and coefficient 0.438 for $z = (0.6, 0.73)$. Though there is a potentially small correlation between SDSS DR7 and the BOSS point, this small correlation is assumed to be negligible. All other correlations are expected to be zero. The χ^2_{BAO} value is computed in the usual manner.

The CMB shift parameter value used is from WMAP7, $R = 1.725 \pm 0.0184$ at a redshift of $z_* = 1091.3$ [48]. $\chi^2_{\rm CMB}$ is computed in the usual manner. The total likelihood is then

$$\mathcal{L}_{\rm tot} \propto e^{-\chi^2_{\rm tot}/2}, \tag{3.9}$$

where $\chi^2_{\rm tot} = \chi^2_{\rm SNe} + \chi^2_{\rm BAO} + \chi^2_{\rm CMB}$.

3.4 Analysis Techniques

In the case of a constant w and the $w_0 - w_a$ parameterizations, a brute-force method is used, where the likelihood of each parameter combination is calculated along a multi-dimensional grid along parameter space [1].

In the case of the principal component parameterization of $w(a)$, a Markov Chain Monte Carlo (MCMC; e.g. see [16, 21]) algorithm is used to place constraints on the cosmological parameters, using a code developed specifically for this purpose. The MCMC code is based on the Metropolis-Hastings algorithm [56, 30], which estimates the posterior distribution of the parameters with the datasets provided to the algorithm. For a detailed overview of the MCMC algorithm, see Appendix B.

Given the likelihood $\mathcal{L}(\mathbf{x}|\mathbf{p})$ of the dataset $\mathbf{x}$ for a set of cosmological parameters $\mathbf{p}$, the posterior is obtained using Bayes' Theorem

$$\mathcal{P}(\mathbf{p}|\mathbf{x}) = \frac{\mathcal{L}(\mathbf{x}|\mathbf{p})\mathcal{P}(\mathbf{p})}{\int d\mathbf{p}\mathcal{L}(\mathbf{x}|\mathbf{p})\mathcal{P}(\mathbf{p})} \tag{3.10}$$

where $\mathcal{P}(\mathbf{p})$ is the prior probability density. The MCMC algorithm samples the posterior distribution at random points on its surface and allows for the estimation of many of its properties, such as parameter means, covariances, and confidence intervals. The initial 10% of the generated chains are discarded as burn-in, and the resulting chains are analyzed for convergence using a Gelman-Rubin convergence cri-

[1] Credit here is given to Daniel Shafer for this calculation.

terion [28] of $\hat{R} < 1.03$ across four chains. Finally, the chains are smoothed with a Gaussian filter and binned for plotting. As a test, results from the two codes are compared for several simple relevant cases and found to be in excellent agreement.

3.5 Results

In this section, I will review the constraints obtained for the various parameterizations of $w(a)$. The three cases considered in the analysis are

1. A constant equation of state, $w =$ constant,
2. The equation of state parameterized as $w(a) = w_0 + w_a(1 - a)$ [52],
3. The equation of state described with a finite number of PCs [39].

3.5.1 Contant w Parameterization

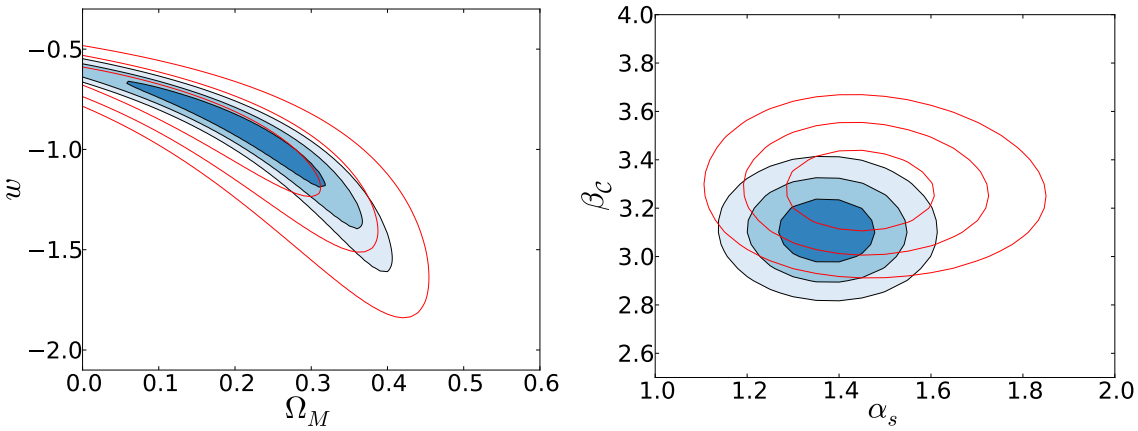

Figure 3.6: Left panel: Constraints in the Ω_M-w plane. Right panel: Constraints in the α_s-β_C plane. Both show the 68.3%, 95.4%, and 99.7% likelihood contours. In both cases, the blue filled contours represent the diagonal-only SN covariance constraints, while the red lines correspond to the full off-diagonal covariance, which includes both the statistical and systematic uncertainties. Only the SN data is used for these constraints, which are marginalized over α_s and β_C for the left panel and Ω_M and w for the right panel.

For this analysis, the relevant parameter space is $\{\Omega_M, w, \alpha_s, \beta_{\mathcal{C}}\}$[2]. The results for the SN-only constraints in the $\Omega_M - w$ plane are shown in the left panel of Fig. 3.6, where the nuisance parameters α_s and $\beta_{\mathcal{C}}$ have been marginalized over. In this figure, the effects of the systematics are shown by overlaying the constraints obtained with the full covariance $\mathbf{C}^{\rm full}$ (red contours) on top of the constraints from the diagonal statistical-only uncertainties $\mathbf{D}^{\rm stat}$ (blue filled contours). The systematics broaden the constraints slightly, though the constraints for each parameter do not change appreciably. The marginalized uncertainty for w is $\sigma_w = 0.17$ for the statistical errors only and $\sigma_w = 0.20$ with the systematics included, increasing the uncertainty in w by only about 20%, even though the total area increase in the $\Omega_M - w$ place is roughly doubled.

Also of interest is the effects of the systematics on the stretch and color nuisance parameters α_s and β_c, since an understanding of these parameters allows for a better understanding into what make SNeIa useful standard candles, and the systematics could potentially affect the constraints on these parameters. The right panel of Figure 3.6 shows the effects in the $\alpha_s - \beta_{\mathcal{C}}$ plane after marginalizing over Ω_M and w. One noteworthy observation is the shift in the color coefficient $\beta_{\mathcal{C}}$, which is shifted to higher values slightly by the systematics, while errors in both parameters are increased by a modest amount.

3.5.2 w_0 and w_a Parameterization

The parameter space is now expanded to include two equation of state parameters: w_0 and w_a. The constraints on these parameters, after marginalizing over Ω_M and the nuisance parameters, are shown in Fig. 3.7. Once again, the constraints from the full systematic covariance $\mathbf{C}^{\rm full}$ is overlaid over the constraints from the statistical-only diagonal uncertainties $\mathbf{D}^{\rm stat}$. The panel on the left shows the constraints from SN

[2]Recall that the nuisance parameter $\mathcal{M}$ is marginalized over analytically, and as such, is not considered a parameter for this analysis.

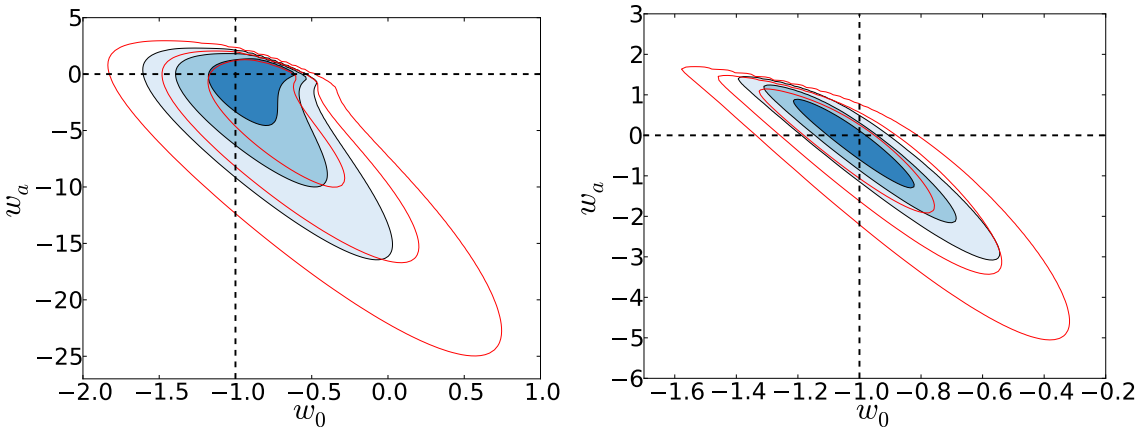

Figure 3.7: Left panel: Constraints in the w_0-w_a plane using only SN data. Right panel: Constraints in the same plane using the combined SN + BAO + CMB datasets. Both show the 68.3%, 95.4%, and 99.7% likelihood contours. In both cases, the blue filled contours represent the diagonal-only SNe covariance constraints, while the red lines correspond to the full off-diagonal covariance, which includes both the statistical and systematic uncertainties. The constraints are marginalized over Ω_M, α_s and $\beta_{\mathcal{C}}$ in both cases. The dashed lines correspond to the ΛCDM values of w_0 (vertial) and w_a (horizontal).

only, while the right includes the information from BAO and CMB as well.

A useful tool to better understand these effects is the figure of merit (FoM), first defined by the Dark Energy Task Force (DETF) [2, 41] as being proportional to the inverse of the area of the 95.4% confidence region A_{95} in the $w_0 - w_a$ plane. Here instead I use the definition as found in Reference [57].

$$\mathrm{FoM}^{(w_0,w_a)} \equiv (\det \mathbf{C})^{-1/2} \approx \frac{6.17\pi}{A_{95}}, \tag{3.11}$$

which becomes exact for a Gaussian posterior distribution, in which this definition agrees with the DETF definition. Table 3.3 shows the FoM for various cases in the $w_0 - w_a$ plane. Overall, the inclusion of systematic uncertainties reduces the FoM by a factor of 2 to 3. These results show explicitly that work needs to be done in reducing the systematic effects, particularly calibration errors, which Reference [18] shows is the biggest source of uncertainty for systematics.

$\mathrm{FoM}^{(w_0\, w_a)}$	$\mathbf{D}^{\mathrm{stat}}$	$\mathbf{C}^{\mathrm{full}}$
SN	2.28	1.16
SN+BAO+CMB	32.9	11.8

Table 3.3: Values of the FoM (defined in Eq. (3.11)) for SN alone (middle row) and SN+BAO+CMB (bottom row). The middle column shows the FoMs for the statistical covariance matrix $\mathbf{D}^{\mathrm{stat}}$ only, while the right column shows the FoMs for the full covariance matrix $\mathbf{C}^{\mathrm{full}}$. Including the systematics reduces the FoM by a factor of 2 to 3.

3.5.3 Principal Component Parameterization

Before presenting the results on the constraints on the PCs, it is important to go over the priors imposed on the PC amplitudes. Top-hat priors are placed on each α_i [58] such that the equation of state is limited to the range $-2 \leq w(z) \leq 0$. This leads to top-hat priors of width [57]

$$\Delta\alpha_i = \frac{2}{N_{\mathrm{PC}}} \sum_{j=0}^{N_z-1} |e_i(z_j)| \tag{3.12}$$

centered around $w(z) = -1$, or $\alpha_i = 0$. Here, N_z is the number of redshift bins for each PC[3]. Later I show that many of these priors are much wider than the ranges allowed on the PC amplitudes by the data, which means that the principal components are mostly unaffected by these priors. This was verified explicitly by constraining the PCs without the priors.

The constraints on all combinations of the 13 parameters (Ω_M, the PC amplitudes α_i, and the nuisance parameters α_s and $\beta_{\mathcal{C}}$) are shown in Fig. 3.8. The black contours represent the constraints using the diagonal statistical SNe uncertainties only, while the red contours represent the constraints using the full SNe covariance. Overall, the systematic uncertainties broaden and shift the contours slightly, as expected.

Fig. 3.9 shows the marginalized constraints on the 10 PC amplitudes only. With

[3]This number is the same as the total number of PCs (36), due to the way they were obtained (see Appendix A for details). However, because only the first 10 PCs are used for the analysis, this distinction is made explicit here.

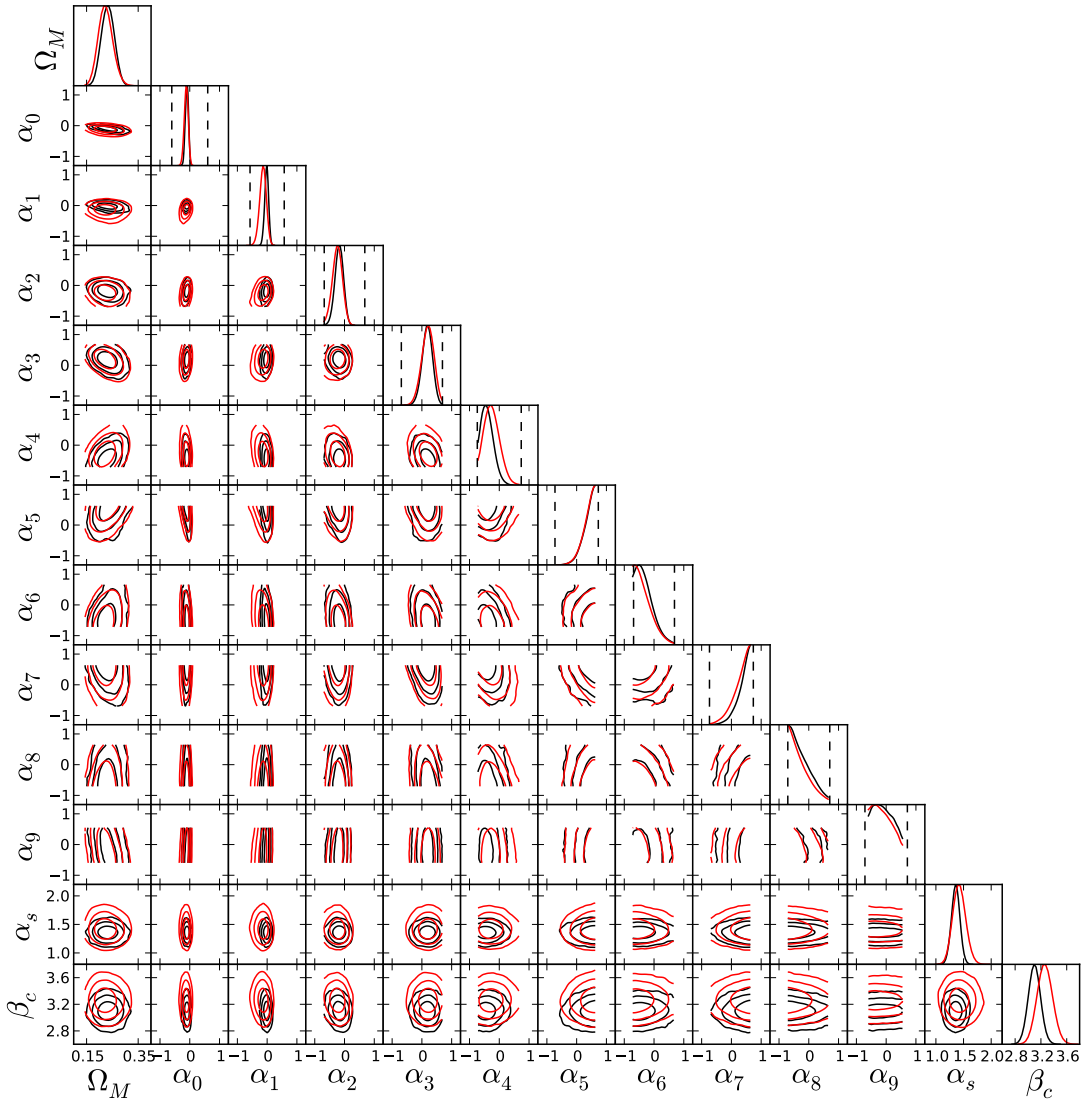

Figure 3.8: The 68.3%, 95.4%, and 99.7% likelihood constraints on all combinations of the 13 cosmological parameters using the combined set of SNe, BAO, and CMB data. The black contours show the constraints in the case of diagonal statistical errors $\mathbf{D}^{\rm stat}$ only, while the red contours show constraints also include the systematic covariance matrix $\mathbf{C}^{\rm sys}$. Priors on the PC amplitudes are shown as dashed vertical lines in the one-dimensional plots. The parameters are ordered: Ω_M, the PC amplitudes $\alpha_0 - \alpha_9$, and the nuisance parameters α_s and $\beta_{\mathcal{C}}$.

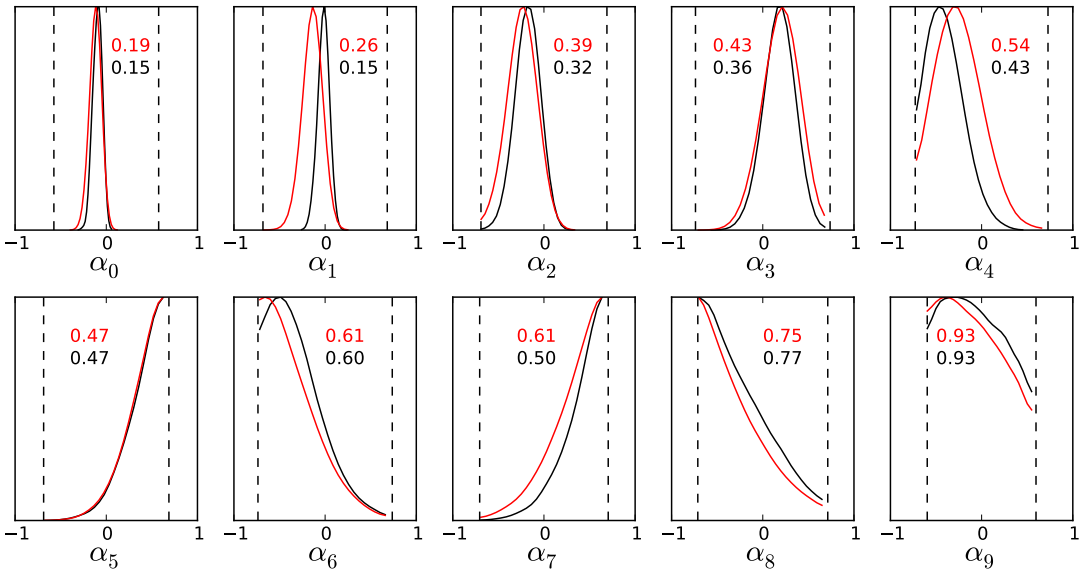

Figure 3.9: The marginalized one-dimensional PC likelihood curves using the combined set of SN, BAO, and CMB data. The black curve shows the likelihood with the diagonal statistical errors only $\mathbf{D}^{\rm stat}$, while the inclusion the systematic covariance matrix $\mathbf{C}^{\rm sys}$ is shown in red. The black and red number in each panel shows the ratio of the PC uncertainty to the rms of the top hat prior for the statistical covariance and full covariance cases, respectivly. The priors are shown as dashed vertical lines.

the diagonal statistical uncertainties only, the first three PCs have a ratio of error to the rms value of the top-hat prior ($\Delta\alpha_i/\sqrt{12}$) of less than 1/3, and six have a ratio of less than 1/2. In the case of the full SNe covariance, two PCs have a ratio of less than 1/3 and five have a ratio of less than 1/2. This shows that the constraints on the PCs are very good with the current data, a result also obtained by Reference [59].

From Fig. 3.9 it's clear that the systematics only slightly broaden the constraints. However, the cumulative effect is not so subtle. Following Reference [57], I define the generalized Figure of Merit

$$\mathrm{FoM}_n^{\rm PC} = \left(\frac{\det \mathbf{C}_n}{\det \mathbf{C}_n^{(\rm prior)}}\right)^{-1/2} \tag{3.13}$$

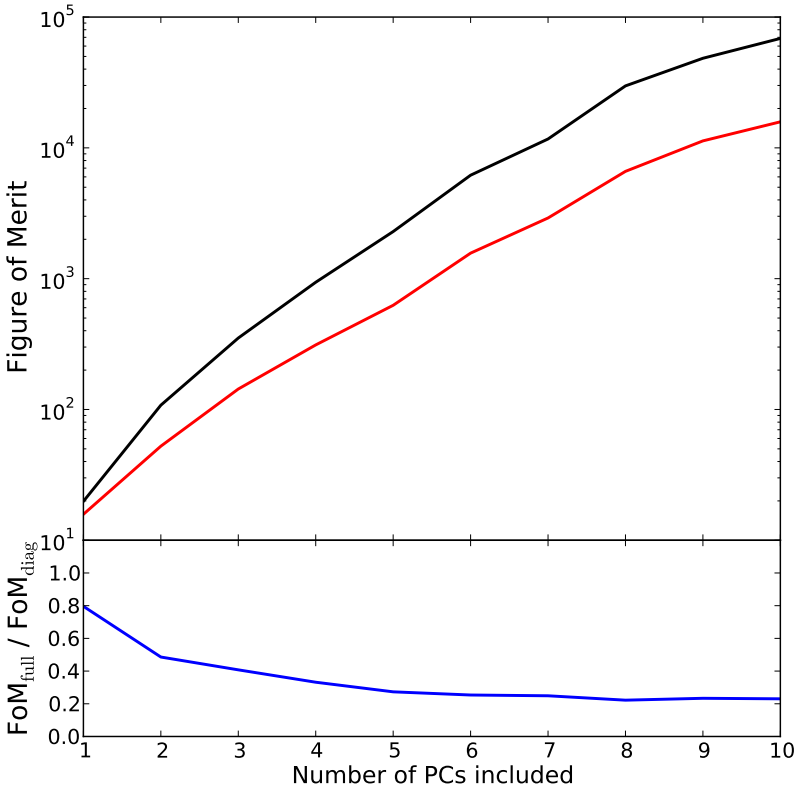

Figure 3.10: Top panel: The Figure of Merit as a function of the number of PCs included, where the black shows the values in the case for the diagonal-only covariance, while the red shows the case for the full covariance. Bottom panel: the ratio of these two Figures of Merit. BAO and CMB data are included in both cases. The FoM ratio levels off after about five PCs have been added.

where $\mathbf{C}_n$ is an $n \times n$ covariance of the first n PCs and

$$\det \mathbf{C}_n^{(\mathrm{prior})} = \prod_{i=0}^{n} \left(\frac{\Delta\alpha_i}{\sqrt{12}} \right)^2 . \tag{3.14}$$

Here, $\Delta\alpha_i/\sqrt{12}$ is again the rms amplitude of the top-hat prior for the ith PC amplitude.

The FoM results are shown in Fig. 3.10, where the FoM is plotted as a function of the number of included PCs. The top panel shows the FoM when constraining with the diagonal statistical-only SN uncertainties (black) and the full covariance including SN systematics (red). The bottom panel shows the ratio of the two cases (blue). The

ratio degrades by a factor of 3 to 4 times as more PCs are included, though it levels off around the fifth PC. This is fortunate, as it is those later PC amplitudes that are harder to constrain, and the systematics seem to only affect the lower PCs. Of course, future surveys may have systematics that behave differently, and may affect more PCs. Once again, these results show that much work is needed in the reduction of systematic uncertainties of future surveys.

3.6 Summary

In this chapter, I have reviewed various alternate parameterizations of the dark energy equation of state $w(z)$. I also went over various systematics obtained by the Supernova Legacy Survey team [18], and gave a brief description of the systematic covariance matrix (see Fig. 3.4). I presented constraints on three different parameterizations of $w(a)$: constant w (Fig. 3.6), $w_0 - w_a$ (Fig. 3.7), and principal components (Fig. 3.8). These constraints were obtained using the SNeIa data along with data from 4 different BAO surveys (see Fig. 3.5), as well from the WMAP7 shift parameter.

I showed the differences in the constraints on the various parameterizations by the SN systematics, and quantified these differences as a reduction of the Figure of Merit. The systematics typically worsened the $w_0 - w_a$ FoM by a factor of $2-3$ (see Table 3.3) and a factor of $3-4$ in the case of the PC parameterization (see Fig. 3.10), though individual parameters in both cases were affected only marginally.

Finally, I showed how the PCs' generalized Figure of Merit changes as a function of the number of PCs included in the calculation, and showed that the ratio of the FoM for the full systematic case over that of the diagonal statistical-only case worsened as more PCs were included, but leveled off after the first few PCs. This indicates that systematics mostly affect the first few PCs, while the later ones remain largely unaffected. Future surveys, with a better understanding of systematics, still remain the key for improvements in constraining dark energy parameters.

CHAPTER 4

A Consistency Test of Dark Energy

4.1 Geometry and Growth as a Test of Dark Energy

As mentioned in Chapter 1, dark energy is just one way to explain the acceleration of the expansion of the universe. A completely different class of explanations are classified under the name modified gravity. In these theories, it is a correction or modification to the equations of general relativity at the largest scales that explains the acceleration. However, these corrections must be suppressed at smaller scales, such as solar-system sized or galactic-sized scales, due to tight constraints on the physics at these scales.

Because gravity is truly modified in these theories, Eq. 1.7 does not describe the growth of structure in the universe. In addition, growth is not necessarily scale-independent. Therefore, for a given an expansion rate $H(t)$, any cosmological distance, or other geometric property, the growth of structure in the universe is predicted to be different for dark energy and modified gravity models.

Comparing the geometric quantities to the growth of structure is therefore an excellent test of the consistency of the DE models, a fact which was pointed out soon after the acceleration was discovered [42, 89, 58, 59, 81]. This is done by separately measuring the redshift evolution of the geometric quantities, constraining the parameters that describe these quantities, and comparing them to equivalent param-

eters that describe the growth of structure. This is similar to other tests done on parameterizing the gravitational potentials Φ and Ψ, which govern non-relativistic (matter) and relativistic (light) motion, and testing whether or not they are the same [91, 6, 93, 35, 19, 20, 77]. The two approaches are complementary to each other.

My goal in this chapter is to perform a major step forward in testing the consistency of dark energy by separately constraining the geometry and growth in cosmological probes of DE. Work similar to this was first performed by References [82] and [1], though the constraints were weak due to the data available at the time. The benefit in this work is the abundance of new data sources and the increase in our knowledge in understanding and modeling them, as well as the addition of new probes not available in 2007. Work done in this Chapter first appeared in Reference [67].

4.2 Geometry and Growth Parameter Split Methodology

The standard ΛCDM model, as well as the more general wCDM model, where the equation of state w is allow to take on other constant values, have been in excellent agreement with observational data since the discovery of the accelerating universe (e.g. [49]), with only the occasional mild warning to the contrary ([71, 14, 87, 74]). However, there has been a large effort to find and test alternative theories, such as the theories of modified gravity, where modifications to the equations that govern gravity can give rise to an accelerating universe.

I take a complementary approach and perform a study of the consistency of the standard wCDM framework. The cosmological parameters that describe the late universe are split into two sets

- Geometry parameters, which dictate the expansion rate $H(z)$ and the comoving distance $r(z)$, as well as any associated values.

- Growth of structure parameters,such as the growth and distribution of density fluctuations ($D(z)$ and $P(k)$, respectively).

The GR framework assumes that the split parameters $X_i^{\rm geom}$ and $X_i^{\rm grow}$, which respectively govern geometry and growth, must be statistically consistent with each other, regardless of the specific parameterization used. Any disagreement between these parameters, outside of any unforeseen systematic errors, can be interpreted as departure from the standard cosmological framework.

This split parameter approach provides a very powerful, but still general, test of wCDM. It can be compared to more specific parameterizations of departures from GR, e.g. the γ parameterization [53], or the comparison of the gravitational potentials described earlier. The split parameter approach is complementary to these methods.

One potential worry is that the information used from the various cosmological probes, usually involving large amounts of raw data, is often compressed into a small number of metaparameters (e.g. the shift parameter R for CMB measurements), and the calculation of these metaparameters sometimes requires the assumption of a cosmological model (an exception to this are SNeIa, which use the raw magnitude data of each supernova). Therefore, the question may arise of whether one should use these metaparameters to constrain a wider class of models where geometry and growth are decoupled. However, for the probes that are only sensitive to either geometry or growth, the metaparameters are *de facto* correct by construction, since they only measure geometry or growth effects. For the probes that are sensitive to both geometry and growth, the metaparameters used are a general enough representation of the raw data that the assumption that geometry and growth are consistent can be relaxed without any loss of robustness and accuracy.

4.3 Data Sources

Due to the nature of the analysis being performed, a variety of data sets that are sensitive to both geometric effects and growth effects are required. The data sources used can be split into two broad categories. The first includes the compilation of Type Ia Supernova magnitude data done by the SNLS team, a variety of BAO data sources from several survey groups, a single measurement of the Shift Parameter from the Planck CMB survey, all of which measure primarily geometric effects. The second group includes measurements of cluster count data from the SDSS MaxBCG Cluster Catalog, weak lensing shear correlation function measurements by the Canada-France-Hawaii Telescope Lensing Survey (CFHTLens), and a collection of RSD measurements from a group of various surveys, all of which are sensitive to both geometric and growth properties of dark energy. A summary of the probes, as well as the portions in which they are sensitive to geometry and growth, can be found in Table 4.1.

Cosmological Probe	Geometry	Growth
SNe Ia	$D_L(z)$	—
BAO	$\left(\frac{D_A^2(z)}{H(z)}\right)^{1/3}/r_s(z_d)$	—
CMB peak loc.	$R \propto \sqrt{\Omega_M H_0^2} D_A(z_*)$	—
Cluster counts	$\frac{dV}{dz}$	$\frac{dn}{dM}$
WL 2 pt. corr.	$\frac{r^2(z)}{H(z)} W_i(z) W_j(z)$	$P\left(k = \frac{\ell}{r(z)}\right)$
RSD	$F(z) \propto D_A(z) H(z)$	$f(z)\sigma_8(z)$

Table 4.1: Summary of cosmological probes used for the consistency test and the aspects of geometry and growth that they are sensitive to.

4.3.1 Supernova Legacy Survey

Similar to in Chapter 3, I use the SNLS data set of 472 SNeIa compiled by Reference [18]. I allow α_s and $\beta_{\mathcal{C}}$ to vary as nuisance parameters, and recalculate full statistical

+ systematic covariance matrix $\mathbf{C}^{\rm full}$ for each new set of values of α_s and $\beta_{\mathcal{C}}$. For this analysis, differences in constraints between statistical-only and statistical + systematic uncertainties are not tested. $\mathcal{M}$ is marginalized over analytically, as before. The χ^2 statistic is again calculated using Eq. 3.8.

4.3.2 BAO Surveys

Because I am interested in testing for both geometric and growth properties of dark energy, I use measurements of $D_V(z)/r_s(z_d)$ (or its inverse) for this analysis, where $D_V(z)$ is the generalized BAO distance measurement and $r_s(z_d)$ is the distance of the sound horizon at the redshift of the drag epoch z_d, as explained in Section 2.4. Three sources of BAO data are used for this analysis: the Six-degree-Field Galaxy Survey (6dFGS) [8], the Sloan Digital Sky Survey Luminous Red Galaxies (SDSS LRG) [60], and the SDSS Baryon Oscillation Spectroscopic Survey (BOSS) [5], summarized in Table 4.2

Survey	$z_{\rm eff}$	Parameter	Measurement
6dFGS [8]	0.106	r_s/D_V	0.336 ± 0.015
SDSS LRG [60]	0.35	D_V/r_s	8.88 ± 0.17
BOSS CMASS [5]	0.57	D_V/r_s	13.67 ± 0.22

Table 4.2: BAO data measurements used here, together with the effective redshift for the corresponding galaxy sample.

Assuming there is no correlation between the different measurements, the χ^2 is simply

$$\chi^2_{\rm BAO} = \sum_i \frac{\left[d_i^{\rm obs} - \bar{d}_i(\mathbf{p})\right]^2}{\sigma_i^2}, \tag{4.1}$$

where $d_i^{\rm obs}$ is the ith data point, $\bar{d}_i(\mathbf{p})$ the ith expectation value given a set of cosmological parameters $\mathbf{p}$, and σ_i the uncertainty in the ith data point.

4.3.3 Planck CMB Survey

To obtain a value of the shift parameter R, I use the Planck collaboration's Planck + WP measurements of r_* and θ_* [63]; since $\theta_* = r_*/D_A(z_*)$, these measurements are marginalized over to get a value for $D_A(z_*)$. Combining this with the Planck values of $\Omega_M h^2$ and z_*, I obtain a value of the Shift Parameter $R = 1.7502 \pm 0.007331$ at a value of the redshift of last scattering at $z_* = 1090.48$. $\chi^2_{\rm CMB}$ is then calculated in the usual manner.

4.3.4 MaxBCG Galaxy Catalog

The MaxBCG Cluster Catalog [66], which was created using measurements done by SDSS, is used for the consistency test. Due to the complexity of this probe, the details of the dataset, including the vector of observables and how to calculate the covariance between data points, can be found in Appendix C.

4.3.5 CFHT Lensing Survey

The Canada-France-Hawaii Telescope Lensing Survey (CFHTLens) [25, 31] provides an excellent source of observational data for the purposes of this test. The survey covers 154 square degrees of the sky and has a mean redshift of $z_{\rm mean} \simeq 0.75$, providing an substantial volume extremely well suited for testing the geometric effects of weak lensing. In addition, this volume includes within it many galaxies with which we can measure the shear correlation function, which provides an excellent source of data regarding the growth of structure of the universe. With measurements in five bands ($ugriz$) and a resolved galaxy density of 17/arcmin^2, the CFHTLens dataset is perfectly suited for the task.

The `blue_sample` dataset, found at the CFHTLens website[1], is used, which was

[1] `http://www.cfhtlens.org/astronomers/content-suitable-astronomers`

shown in Reference [31] to have a negligible intrinsic alignment signal, a common source of error for weak lensing. The dataset contains values of the two-point correlation function $\xi_\pm$ as defined in Eq. (2.34). Each correlation function is divided into 6 tomographic redshift bins and presented at five angles. This results in $2 \times [(6 \times 7)/2] \times 5 = 210$ total data points. In addition, the CFHTLens team computed a 210×210 covariance matrix $C_{\rm WL}$ using numerical simulations, also available on their website. The χ^2 statistic for WL is

$$\chi^2_{\rm WL} = \left[\xi^{\rm obs} - \bar{\xi}(\mathbf{p})\right]^T C^{-1}_{\rm WL} \left[\xi^{\rm obs} - \bar{\xi}(\mathbf{p})\right], \tag{4.2}$$

where $\xi^{\rm obs}$ is the data vector of WL data and $\bar{\xi}(\mathbf{p})$ is the vector of expectation values for the correlation function for a set of cosmological parameters $\mathbf{p}$.

4.3.6 RSD Surveys

z	Parameter	Measurement (diag)	Survey
0.067	$f\sigma_8$	0.42 ± 0.06	6dFGS [9]
0.32	$H(z)$	78.1 ± 7.1	BOSS LOWZ [17]
0.32	$D_A(z)$	950 ± 61	BOSS LOWZ [17]
0.32	$f\sigma_8$	0.38 ± 0.10	BOSS LOWZ [17]
0.44	$F(z)$	0.48 ± 0.05	WiggleZ [12]
0.44	$f\sigma_8$	0.41 ± 0.08	WiggleZ [12]
0.57	$H(z)$	97.1 ± 5.5	BOSS CMASS [17]
0.57	$D_A(z)$	1351 ± 60	BOSS CMASS [17]
0.57	$f\sigma_8$	0.38 ± 0.04	BOSS CMASS [17]
0.60	$F(z)$	0.65 ± 0.05	WiggleZ [12]
0.60	$f\sigma_8$	0.39 ± 0.06	WiggleZ [12]
0.73	$F(z)$	0.87 ± 0.07	WiggleZ [12]
0.73	$f\sigma_8$	0.44 ± 0.07	WiggleZ [12]

Table 4.3: RSD measurements from the three surveys used in this analysis. Each line shows the effective redshift of the data point, the parameter measured, the value of that parameter and its associated diagonal error, and the survey the data point comes from. Measurements from the same survey are correlated; for the correlation matrices see Tables 4.4 and 4.5.

Redshift space distortions are also perfectly suited for the task of testing for con-

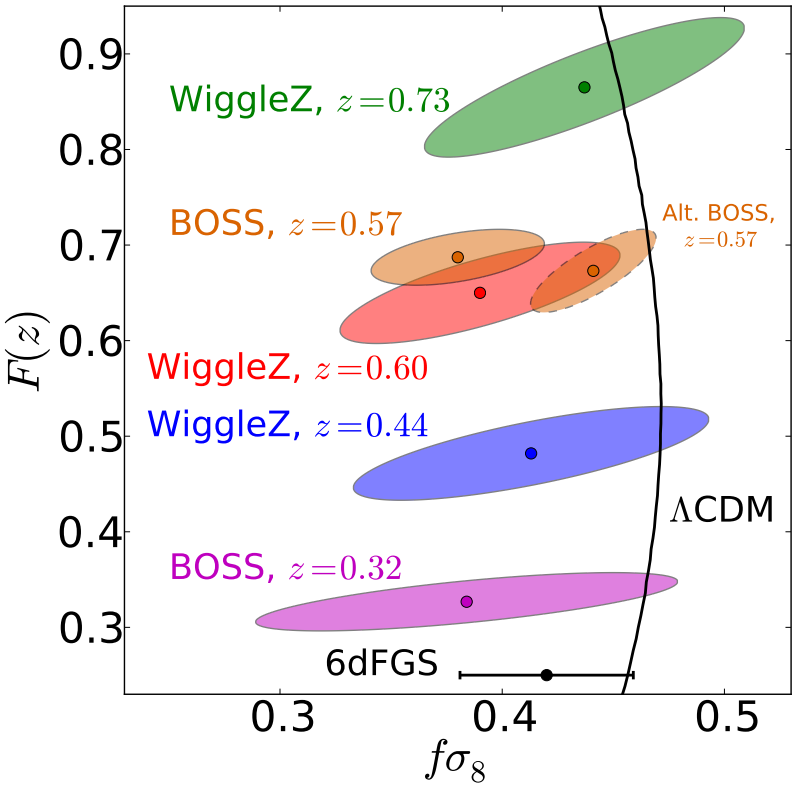

Figure 4.1: RSD data used in the analysis, along with the $1-\sigma$ error contours, shown in the $f\sigma_8$–F plane; more details can be found in Table 4.3. The black line shows the best fit ΛCDM model with the mean parameter values given in the second column of Table 4.8. The 6dFGS measurement does not have an associated value for $F(z)$, so only its horizontal error bar is shown. The BOSS constraints on $F(z)$ are obtained from the covariance of $H(z)$ and $D_A(z)$. The point with the dashed error ellipse corresponds to an alternative RSD measurement at $z = 0.57$ from Reference [69]; for details, see Section 4.6.

sistency of DE, since they measure both geometric and growth properties. An assortment of RSD data points from three surveys are used (6dFGS [9], BOSS [17], and WiggleZ [12]), which provide values for $f\sigma_8$ and either $F(z)$ or $H(z)$ and $D_A(z)$. The data are shown in Table 4.3 and plotted in Figure 4.1. Data points from the same survey are also correlated; the correlation matrices for these are shown in Tables 4.4 and 4.5. The χ^2 statistic is calculated in the usual manner, similar to the other probes.

$z = 0.32$	$H(z)$	$D_A(z)$	$f\sigma_8$
$H(z)$	1.00	-0.32	0.35
$D_A(z)$	—	1.00	0.51
$f\sigma_8$	—	—	1.00

$z = 0.57$	$H(z)$	$D_A(z)$	$f\sigma_8$
$H(z)$	1.00	-0.67	0.05
$D_A(z)$	—	1.00	0.40
$f\sigma_8$	—	—	1.00

Table 4.4: Correlation matrices for the BOSS LOWZ (left) and CMASS (right) samples of the RSD dataset. The values of the diagonal entries of the covariance can be found in Table 4.3.

	$F(0.44)$	$F(0.60)$	$F(0.73)$	$f\sigma_8(0.44)$	$f\sigma_8(0.60)$	$f\sigma_8(0.73)$
$F(z = 0.44)$	1.00	0.52	0.00	0.73	0.35	0.00
$F(z = 0.60)$	—	1.00	0.50	0.38	0.74	0.43
$F(z = 0.73)$	—	—	1.00	0.00	0.43	0.85
$f\sigma_8(z = 0.44)$	—	—	—	1.00	0.51	0.00
$f\sigma_8(z = 0.60)$	—	—	—	—	1.00	0.56
$f\sigma_8(z = 0.73)$	—	—	—	—	—	1.00

Table 4.5: Correlation matrix for the WiggleZ sample of the RSD dataset. The values of the diagonal entries of the covariance can be found in Table 4.3.

4.4 Parameters and Analysis

4.4.1 Parameter Space and Priors

Based on the probes involved, the set of fundamental cosmological used for this analysis is

$$\vec{\mathbf{p}}^{\text{fund}} = \{\Omega_M, \Omega_M h^2, \Omega_B h^2, w, 10^9 A, n_s\}. \tag{4.3}$$

In addition, the set of nuisance parameters is

$$\vec{\mathbf{p}}^{\text{nuis}} = \{\alpha_s, \beta_{\mathcal{C}}, \langle \ln N | M_1 \rangle, \langle \ln N | M_2 \rangle, \sigma_{NM}, \beta\}. \tag{4.4}$$

Recall that α_s and $\beta_{\mathcal{C}}$ are the supernova stretch and color nuisance parameters, while the remaining four are the cluster nuisance parameters. Also included in the analysis are the derived parameters

$$\vec{\mathbf{p}}^{\text{deriv}} = \{\sigma_8, h; \sigma_{MN}\}, \tag{4.5}$$

where the parameters are divided into cosmological (first two) and nuisance (last) parameters. Here, σ_{MN} is the scatter of the richness of galaxy clusters for a given mass, as opposed to σ_{NM}, which is the scatter of galaxy cluster masses for a given richness, and is calculated using the equation

$$\sigma_{MN} = \frac{\sigma_{NM} \log_{10}(M_2/M_1)}{\langle \ln N|M_2\rangle - \langle \ln N|M_1\rangle}, \tag{4.6}$$

which is derived using the propagation of uncertainty relations on Eq. 2.32

The analysis assumes a constant equation of state and a flat universe. In addition, the sum of neutrino masses (which appears in the calculation of the transfer function) is set to $m_\nu = 0.06$ eV, which is consistent with atmospheric and solar data on neutrino flavor oscillations and a normal hierarchy between the individual mass eigenstates [7]. Note that the mass sum is allowed to vary in the extended tests in Sec. 4.6. The number of neutrino species is held fixed at $N_\nu = 3.046$ throughout the analysis, as predicted by the Standard Model.

Priors on Ω_M, σ_{NM}, β, and σ_{MN} are adopted from Reference [66]. In addition, weak, flat priors are imposed on w, n_s, and h. Finally, a multidimensional Gaussian prior on $\Omega_M h^2$, $\Omega_B h^2$, $10^9 A$, and n_s is imposed, which is referred to as the "Early Universe" (EU) prior. Details for all priors can be found in Tables 4.6 and 4.7.

4.4.2 A Note on Possible Correlations Between Probes

The total likelihood of the combined probes is the product of the individual likelihoods $\mathcal{L} = e^{-\chi^2/2}$

$$\mathcal{L} = \mathcal{L}_{\rm SN}\mathcal{L}_{\rm BAO}\mathcal{L}_{\rm CMB}\mathcal{L}_{\rm clusters}\mathcal{L}_{\rm WL}\mathcal{L}_{\rm RSD}. \tag{4.7}$$

The assumption that the individual likelihoods are uncorrelated may come into question, but it is well justified given the nature of the datasets used. The CMB shift parameter is decoupled from all other probes due to the high redshift of the mea-

Parameter	Priors	Geometry	Growth
Ω_M	[0.05, 0.95]	✓	✓
$\Omega_M h^2$	0.1423 ± 0.0029		✓
$\Omega_B h^2$	0.02207 ± 0.00033		✓
w	[-2, 0]	✓	✓
$10^9 A$	2.215 ± 0.16		✓
n_s	[0.9, 1.1], 0.9616 ± 0.0094		✓
σ_8	—		✓
h	[0.5, 1.0]		✓

Table 4.6: Cosmological parameters used in the analysis. The first seven parameters are the fundamental parameters varied in the MCMC, while the next two parameters are derived from those fundamental parameters. In the 'Priors' column, $[a, b]$ indicates a flat prior between the end points a and b, while $c \pm d$ refers to a Gaussian prior with mean c and standard deviation d. The Gaussian priors on $\Omega_M h^2$, $\Omega_B h^2$, $10^9 A$, and n_s are the diagonal quantities of the early-universe prior, more information of which can be found in Table 4.7. Whether the parameter is included in the geometry and growth components of equations is indicated by the last two columns; if a parameter is found in both, it is considered a split parameter. In addition to the parameters shown here, there are a number of probe-specfic nuisance parameters: see text for details.

surement. Similarly, cluster counts, which can be thought of as a 1-point correlation function, are only coupled to the two-point function via very small second order effects. Weak lensing and SN are thought to be correlated, since supernovae are lensed, but the effect is very small for the current set of data.

Of biggest concern is the correlation between BAO and RSD, as these are measured in similar redshift ranges, and, in the case of both WiggleZ and BOSS, use the same galaxies. This correlation is due to the RSD's sensitivity to the Alcock- Paczynski parameter combination $F(z) \propto D_A(z)H(z)$. These in turn may be slightly degenerate with BAO measurements. However, measurements by these teams show that the correlation between these measurements are small at only the 10% level [17, 12]. Thus, multiplying the individual likelihoods is justified.

	$\Omega_M h^2$	$\Omega_B h^2$	$10^9 A$	n_s
$\Omega_M h^2$	1.00	−0.62	−0.51	−0.84
$\Omega_B h^2$	—	1.00	0.56	0.70
$10^9 A$	—	—	1.00	0.65
n_s	—	—	—	1.00

Table 4.7: Correlation matrix corresponding to the early-universe prior (labeled as "EU" in plots). The correlation matrix is calculated from Planck ΛCDM (+ lowl) MCMC chains [63]. The square roots of the diagonal entries of the full covariance matrix prior are shown in Table 4.6. The full prior covariance is applied to RSD, WL and clusters, and the overall combined constraint. In the case of BAO, only the information from the 2×2 subset containing $\Omega_M h^2$ and $\Omega_B h^2$ is applied, corresponding to the sound horizon ("SH" in plots). Neither prior is applied for SN and CMB constraints.

4.4.3 Analysis Technique

Similar to the analysis in Chapter 3, an MCMC algorithm is used to place constraints on the cosmological parameters (see Appendix B for more information on the MCMC algorithm), with a code developed specifically for this purpose, based on the code used for the PC constraints. A parameter covariance matrix is calculated by performing a few shorter runs to optimize the MCMC step size and direction and minimize overall runtime. The initial 10% of the chains are thrown out, and the chains are analyzed for convergence using a Gelman-Rubin convergence criterion [28] of $\hat{R} < 1.03$ across a minimum of six chains. The resulting chains are binned and smoothed with a Gaussian filter for plotting.

4.5 Results

4.5.1 Unsplit Case

Before any parameter splits are made, the fiducial unsplit constraints are shown to make sure they are in agreement with similar recent constraints. The left panel of Fig. 4.2 shows the marginalized constraints in the $\Omega_M - \sigma_8$ plane for the ΛCDM case

Parameter	Unsplit, $w=-1$	Unsplit, w varied	Split, $w=-1$	Split, w varied
$\Omega_M \begin{cases} \Omega_M^{\rm geom} \\ \Omega_M^{\rm grow} \end{cases}$	0.303 ± 0.008	0.299 ± 0.010	0.302 ± 0.008 0.321 ± 0.017	0.283 ± 0.011 0.311 ± 0.017
$\Omega_M h^2$	0.140 ± 0.001	0.141 ± 0.002	0.140 ± 0.001	0.142 ± 0.002
$\Omega_B h^2$	0.0221 ± 0.0002	0.0220 ± 0.0003	0.0221 ± 0.0002	0.0221 ± 0.0003
$w \begin{cases} w^{\rm geom} \\ w^{\rm grow} \end{cases}$	—	-1.03 ± 0.05	— —	-1.13 ± 0.06 -0.77 ± 0.08
$10^9 A$	1.95 ± 0.09	1.91 ± 0.10	1.96 ± 0.09	2.17 ± 0.13
n_s	0.961 ± 0.005	0.959 ± 0.006	0.962 ± 0.005	0.961 ± 0.006
σ_8	0.786 ± 0.015	0.788 ± 0.016	0.782 ± 0.016	0.771 ± 0.017
h	0.680 ± 0.006	0.687 ± 0.012	0.661 ± 0.017	0.677 ± 0.018
α_s	1.44 ± 0.11	1.44 ± 0.11	1.44 ± 0.11	1.44 ± 0.11
β_c	3.26 ± 0.11	3.26 ± 0.11	3.26 ± 0.11	3.27 ± 0.11
$\ln(N\|M_1)$	2.36 ± 0.06	2.37 ± 0.06	2.29 ± 0.08	2.33 ± 0.08
$\ln(N\|M_2)$	4.15 ± 0.09	4.16 ± 0.09	4.09 ± 0.11	4.15 ± 0.11
σ_{NM}	0.359 ± 0.057	0.357 ± 0.057	0.378 ± 0.059	0.367 ± 0.060
β	1.041 ± 0.050	1.045 ± 0.051	1.018 ± 0.054	1.036 ± 0.055
σ_{MN}	0.462 ± 0.081	0.459 ± 0.082	0.486 ± 0.085	0.464 ± 0.084

Table 4.8: Constraints on the cosmological parameters from the combined probes. The second column shows constraints in the unsplit ΛCDM ($w=-1$) model, while the third column also shows the standard unsplit case but allows w to vary. The fourth and fifth columns are main results, and show the split-parameter cases where Ω_M is split and $w^{\rm geom} = w^{\rm grow} = -1$ is fixed (fourth column), and finally where both Ω_M and w are split and allowed to vary (fifth column). In cases of parameters that can be split, the constraints are given either on the unsplit parameter (vertically centered number) or separate constraints on the geometry and growth split parameters (vertically offset pair of numbers).

($w=-1$), while the right panel shows the constraints in the $\Omega_M - w$ plane. Already, the complementarity of the probes is evident: SN, BAO, and CMB are particularly sensitive to geometry, so they constrain Ω_M and w rather well; the same cannot be said about their constraints on σ_8, which they can't measure at all. Clusters, WL, and RSD, however, are excellent probes of growth, and (in the ΛCDM case) constrain the characteristic combinations

$$\begin{aligned} (\Omega_M/0.3)^{0.28}\sigma_8 &= 0.799 \pm 0.018 \quad \text{(WL)}, \\ (\Omega_M/0.3)^{0.04}\sigma_8 &= 0.809 \pm 0.022 \quad \text{(RSD)}, \\ (\Omega_M/0.3)^{0.27}\sigma_8 &= 0.837 \pm 0.021 \quad \text{(clusters)}. \end{aligned} \tag{4.8}$$

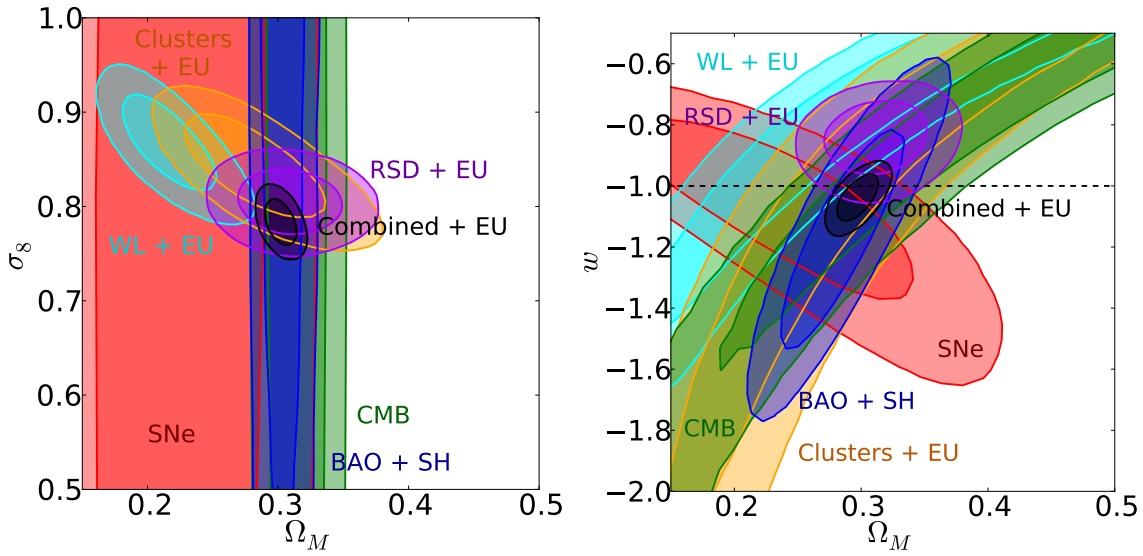

Figure 4.2: Constraints from cosmological probes before the geometry-growth parameter split. Shown are the 68% and 95% confidence constraints in the Ω_M–σ_8 plane assuming $w = -1$ held constant (left panel) and in the Ω_M-w plane (right panel). For the labels, "EU" refers to the early universe prior, while "SH" refers to the sound horizon prior; see Table 4.7 for details.

To obtain these best-constrained combinations of Ω_M and σ_8, the power α was varied until the error of the quantity $(\Omega_M/0.3)^\alpha\sigma_8$ was minimized.

An interesting observation are the constraints from the RSD in the $\Omega_M - w$ plane in Fig. 4.2, which tend to slightly prefer higher values of w than the ΛCDM value, corresponding to less growth in the late universe than expected in ΛCDM. This preference for RSD is also apparent in the data, as shown in Fig. 4.1, where the RSD points prefer lower values of $f\sigma_8$ compared to the ΛCDM case. This preference will have impacts later when the dark energy parameters are split.

Another thing to note is that WL constraints favor a somewhat lower value of Ω_M and a higher value of σ_8 than those favored by the other datasets. This has been noted by Reference [55], where possible reasons for this parameter tension are discussed. Since weak lensing is currently less mature than many of the other cosmological probes, and the fact that it only weakly contributes to our principal constraints discussed below, this point is not discussed further.

The final combined constraints on Ω_M and w are

$$\begin{aligned} \Omega_M &= 0.299 \pm 0.010 \\ w &= -1.03 \pm 0.05 \end{aligned} \qquad \text{(unsplit case)} \tag{4.9}$$

Constraints on the other parameters can be found in the third column[2] of Table 4.8.

4.5.2 Split Ω_M only

For this case, Ω_M is split into two parameters: $\Omega_M^{\rm geom}$ and $\Omega_M^{\rm grow}$. w is held constant at the ΛCDM value ($w = -1$). The rest of the cosmological parameters ($\{\Omega_M h^2, \Omega_B h^2, 10^9 A, n_s\}$) are also allowed to vary, as well as the nuisance parameters. The constraints are shown in Fig. 4.3 and the fourth column of Table 4.8.

Certain things here are expected: CMB and BAO only probe geometry, both preferring $\Omega_M^{\rm geom} \simeq 0.3$. Recall that the BAO constraints also include the SH prior, otherwise, it would be much weaker. SN also only constrain geometry, and though they prefer slightly lower value, the errors are still large enough to encompass the $\Omega_M^{\rm geom} = 0.3$ value at $2-\sigma$.

It is somewhat surprising that clusters constrain growth much more than geometry, even though they are sensitive to both (see Table 4.1). This is good news, since constraints on growth are usually weaker than on geometry. Overall, the cluster constraint on $\Omega_M^{\rm grow}$ is roughly consistent with the values $0.25 - 0.30$. Likewise, RSD are more sensitive to growth over geometry, with similar constraints on $\Omega_M^{\rm grow}$. The constraints from WL are not as tight as its counterparts, but nonetheless constrain geometry fairly well, though constraints on growth are somewhat poor.

The combined constraints show how the probes greatly complement each other. If anything, this shows the remarkable progress in the field since similar constraints

[2]For completeness, the constraints on the unsplit case with $w = -1$ held fixed are shown in the second column of the same Table.

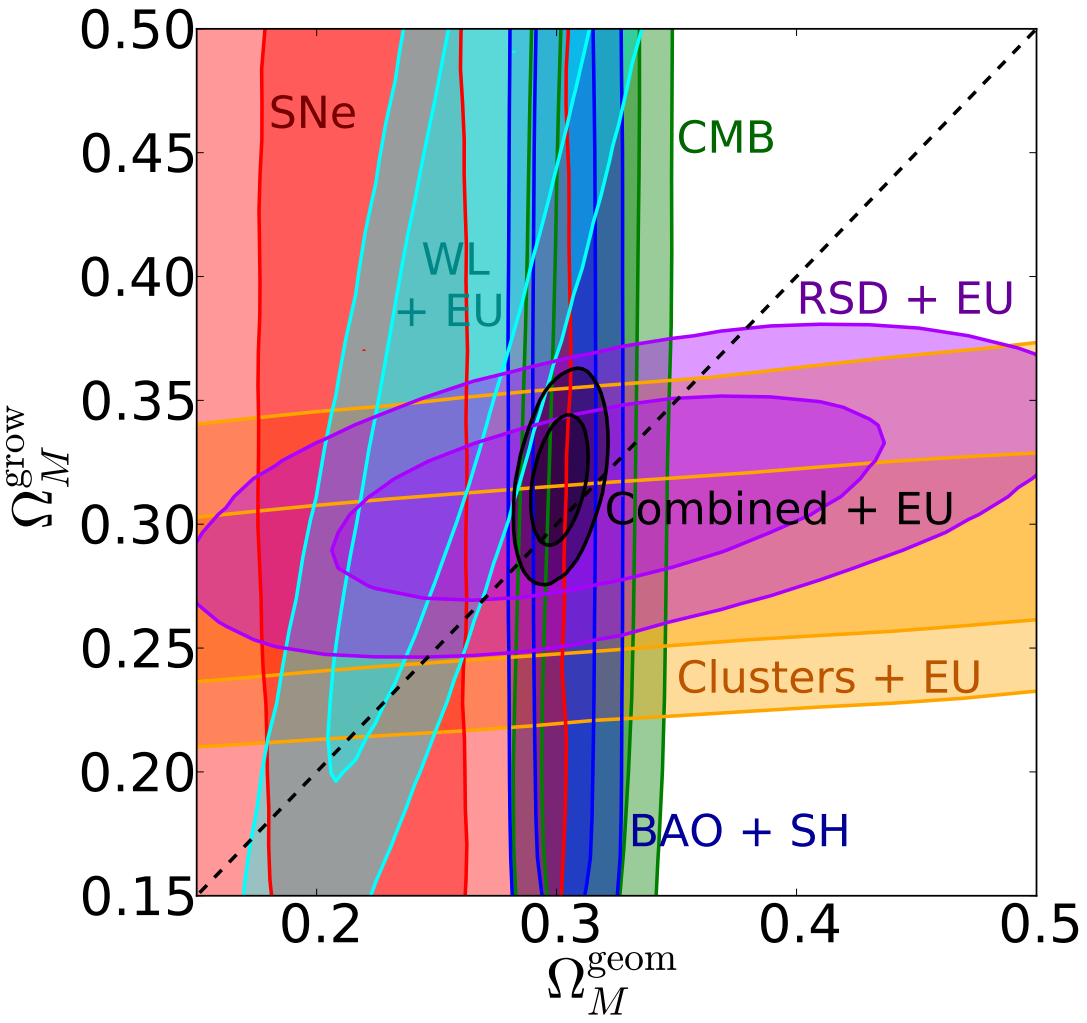

Figure 4.3: 68% and 95% confidence constraints in the split Ω_M plane with the equation of state held constant at the ΛCDM value ($w^{\rm geom} = w^{\rm grow} = -1$). Just like in Fig. 4.2, "EU" refers to the early universe prior, while "SH" refers to the sound horizon prior.

were done by Reference [82]. The marginalized combined constraints on the split Ω_M's are

$$\begin{aligned} \Omega_M^{\rm geom} &= 0.302 \pm 0.008 \\ \Omega_M^{\rm grow} &= 0.321 \pm 0.017 \end{aligned} \qquad (\Omega_M \text{ split}, w = -1) \tag{4.10}$$

In this case, the geometry and growth constraints are clearly consistent with each other, though the geometry constraint is stronger, as is expected.

4.5.3 Split Ω_M and w

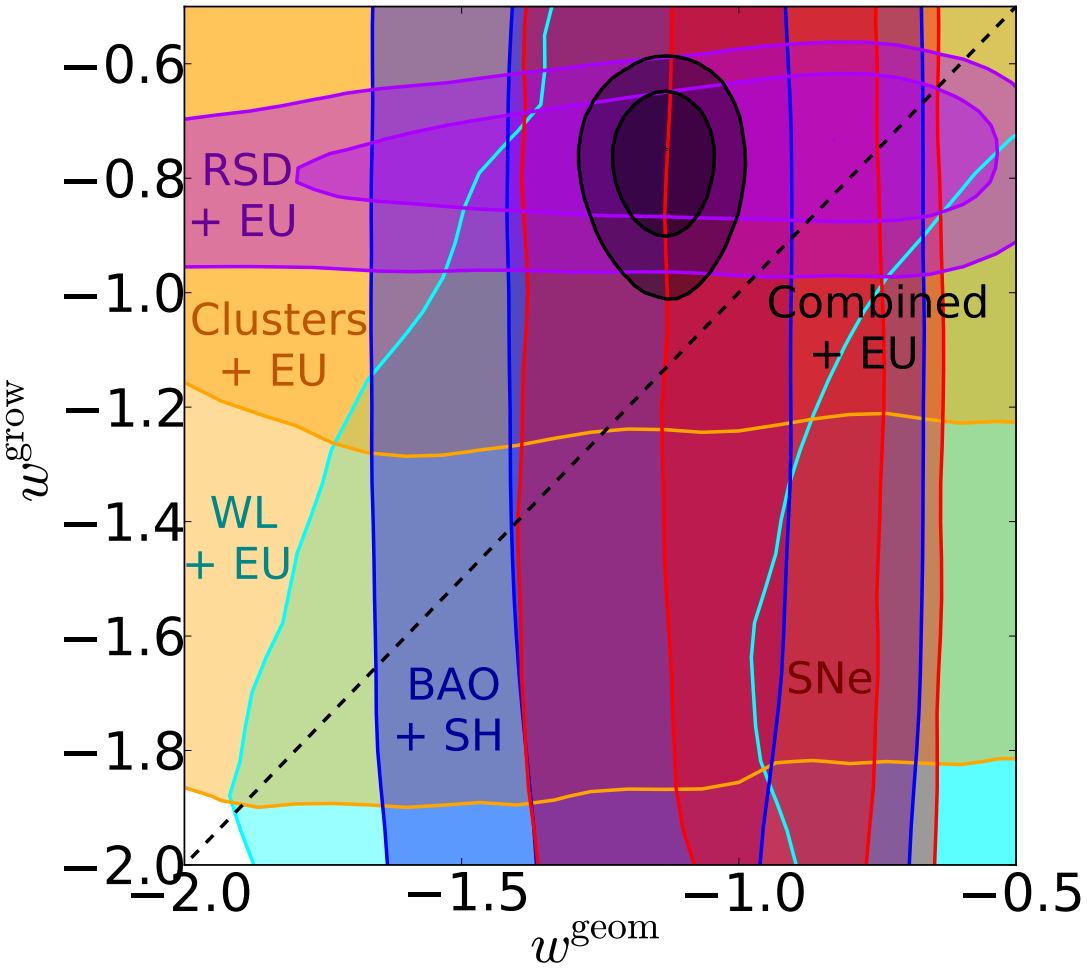

Figure 4.4: 68% and 95% confidence constraints in the split w plane. As before, "EU" refers to the early universe prior, while "SH" refers to the sound horizon prior. Due to the poor constraints from the CMB, they are not shown in this figure.

A much more difficult task involves constraining the geometry and growth components of both the matter energy density and the equation of state, since this now involves a total of four split parameters, $\{\Omega_M^{\rm geom}, \Omega_M^{\rm grow}, w^{\rm geom}, w^{\rm grow}\}$. Due to the degeneracies involved, every probe used in an invaluable asset, given that they break degeneracies in the 15-dimensional parameter space, which leads to excellent combined constraints.

Fig. 4.4 shows the constraints in the split-w plane, marginalized over the cos-

mological parameters $\{\Omega_M^{\rm geom}, \Omega_M^{\rm grow}, \Omega_M h^2, \Omega_B h^2, 10^9 A, n_s\}$, as well as the nuisance parameters. As before, the constraints are largely in the directions expected, though the constraints are expectedly weaker due to marginalizing over $\Omega_M^{\rm geom}$ and $\Omega_M^{\rm grow}$. BAO and SN still constrain geometry reasonably well, though the CMB do rather poorly in this space, mainly since it is only a single point of data, and thus subject to degeneracies between $\Omega_M^{\rm geom}$ and $w^{\rm geom}$ (due to this, the constraints from the CMB are not shown in Fig. 4.4). Similarly, WL and clusters constrain both geometry and growth weakly, though the constraints on growth from clusters are much stronger than its constraints on geometry, as before.

The one outlier are the RSD. Alone, they are able to constrain growth very precisely, but do so at a value

$$w^{\rm grow,RSD} = -0.760 \pm 0.085, \tag{4.11}$$

which is far from the ΛCDM value of -1. As mentioned previously, this higher value of w from the RSD correspond to a supression of the growth of structure in late times compared to the ΛCDM prediction. It is clear from Fig. 4.4 that the RSD are pulling the combined constraint toward this higher growth value. This leads marginalized combined constraints

$$\begin{aligned} \Omega_M^{\rm geom} &= 0.283 \pm 0.011 \\ \Omega_M^{\rm grow} &= 0.311 \pm 0.017 \\ w^{\rm geom} &= -1.13 \pm 0.06 \\ w^{\rm grow} &= -0.77 \pm 0.08 \end{aligned} \qquad (\Omega_M \text{ and } w \text{ both split}) \tag{4.12}$$

with the rest of the constraints on parameters can be found on Table. 4.8. The goodness of fit with and without RSD is also satisfactory: with RSD $\chi^2/{\rm dof} = 728/699 = 1.04$, and when the RSD are removed, $\chi^2/{\rm dof} = 719/686 = 1.05$.

The significance of the pull away from the $w^{\rm geom} = w^{\rm grow}$ can be quantified using a p-value, calculated using the equation

$$p = \frac{\int_{w^{\rm geom}>w^{\rm grow}} dw^{\rm geom} dw^{\rm grow} \mathcal{L}(w^{\rm geom}, w^{\rm grow})}{\int dw^{\rm geom} dw^{\rm grow} \mathcal{L}(w^{\rm geom}, w^{\rm grow})}, \tag{4.13}$$

which is the fraction for the likelihood in which $w^{\rm geom} > w^{\rm grow}$. The p-value is 0.0010 for the combined constraints, corresponding to an inconsistency with the ΛCDM value at 3.3σ[3].

4.6 Discussion

The result of $w_{\rm grow} > -1$ from RSD data is not necessarily a new one: many analyses of RSD data have shown that they are in some tension with ΛCDM at a $> 2-\sigma$ level. For example, Reference [11] finds discrepant measurements of the growth index $\gamma = 0.772^{+0.124}_{-0.097}$, significatly different from the ΛCDM value of $\gamma = 0.55$. Similarly, References [69] and [64] found using RSD measurements that growth seems to be less than expected. Finally, Reference [10] finds evidence for a non-zero neutrino mass using RSD, once again evidence for physics beyond the standard model.

The first scenario investigated is how the results depend on the choice of RSD analyses. Even within BOSS, different analyses make different assumptions and give somewhat different results; this is best shown for the $z = 0.57$ measurements shown in Fig. 4.1. To avoid the *a posteriori* bias of hand-picking analyses that give results that are closer, or further away, from the concordance ΛCDM model, the original choice of the RSD data from Fig. 4.1 and Table 4.3 is kept as fiducial. As an alternative, the measurement at $z = 0.57$, which clearly is most responsible for the discrepancy with the standard cosmological model, is replaced by the alternative analysis of the

[3]The p-value is assumed to represent one tail of a two-sided Gaussian distribution for the calculation of the number of "sigmas"; it would have been equally as surprising to obtain the opposite result, namely $w^{\rm grow} > w^{\rm geom}$, and so this more conservative number of σ's seems appropriate.

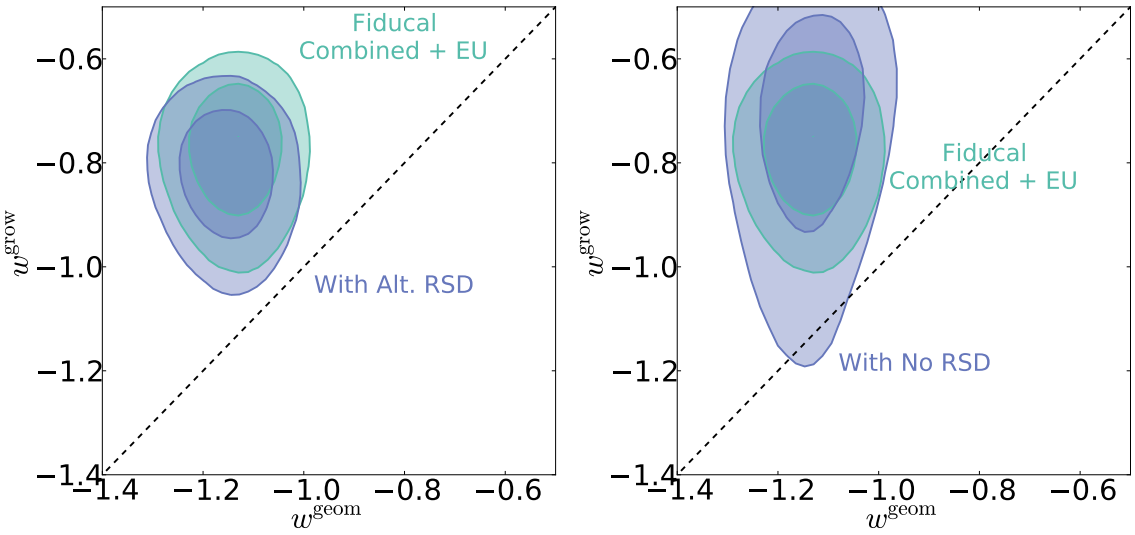

Figure 4.5: Dependence of the results on the RSD data and their analyses. Left panel: Combined constraints for the case where the $z = 0.57$ RSD measurement from [17] is replaced with the alternative BOSS measurement that uses the same raw data but a different analysis [69]; see Fig. 4.1. The combined constraints are now only slightly less discrepant with the $w^{\rm geom} = w^{\rm grow}$ line; see text for details. Right panel: Combined constraints, but with the RSD data fully excluded. The combined contour is now larger in the growth direction; however it is still somewhat discrepant with the w geom = w grow line, though less so than with the RSD data included.

same data [69] that gives the measurements of $(F, f\sigma_8)$ at $z = 0.57$ that are less discrepant with the ΛCDM model (see Fig. 4.1), and the resulting combined analysis is investigated.

The results are shown in the left panel of Fig. 4.5. The combined constraints (RSD + everything else) are now slightly closer to the geometry=growth line, but the p-value is still small (0.0020), indicating a 3.1-σ discrepancy with the geometry=growth prediction. The constraints on cosmological parameters with this alternate RSD $z = 0.57$ measurement from BOSS are

$$\begin{aligned} \Omega^{\rm geom} &= 0.279 \pm 0.011 \\ \Omega^{\rm grow} &= 0.319 \pm 0.021 \\ w^{\rm geom} &= -1.14 \pm 0.06 \\ w^{\rm grow} &= -0.81 \pm 0.08 \end{aligned} \qquad \text{(alternate RSD).} \tag{4.14}$$

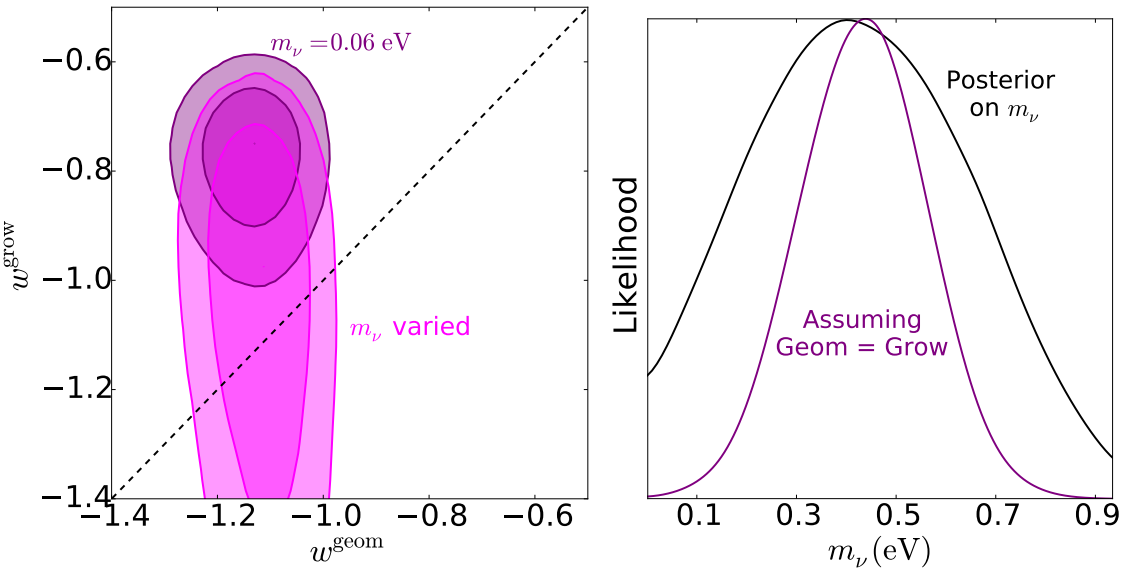

Figure 4.6: Left panel: The effects on the combined constraints when the sum of the neutrino masses m_ν is allowed to vary, compared to the fiducial assumption of holding it fixed at 0.06 eV. The constraints are now fully consistent with the $w^{\rm geom} = w^{\rm grow}$ line. Right panel: The posterior likelihood on m_ν for when Ω_M and w are split (wider curve) and when geometry = growth is enforced (narrower curve). For both cases, the preferred value is $m_\nu \simeq 0.45$ eV; see text for details.

Once again, the RSD pull the combined constraints towards less growth in the late universe. The goodness-of-fit for this case is also satisfactory, $\chi^2/{\rm dof} = 724/699 = 1.04$.

The effects of removing the RSD from the split-w constraints is also considered, and is shown in the right panel of Fig. 4.5. In this case, the discrepancy with the $w^{\rm geom} = w^{\rm grow}$ expectation is somewhat lower, though the p-value is still somewhat small at 0.0204, corresponding to a discrepancy of 2.3σ. Even with the full removal of the RSD from the analysis, the combined probes still stlightly prefer less growth of structure than expected from ΛCDM, possibly hinting at some underlying effects that may cause the discrepancy.

Of particular interest is the effect of the neutrino mass sum on constraints. Traditionally, cosmology has provided only upper limits to the sum of neutrino masses, roughly $m_\nu \lesssim 0.3$ eV [e.g. 73]. Recently several papers have claimed evidence for a

positive neutrino mass in order to alleviate the discrepancy between the RSD data and the ΛCDM model [10], or the tensions between the local measurements of Hubble constant and Planck data [36, 22].

To test the effect of neutrino mass sum on the combined constraints (including RSD), it is allowed to vary within the range $m_\nu \in [0, 1]$ eV. The combined results are compared to the fiducial case (i.e. $m_\nu = 0.06$ eV); the results are shown in the left panel of Fig. 4.6. Allowing the combined masses of neutrinos to vary results in a significant increase in the range of values allowed by the combined data, and the constraints are fully consistent with the growth=geometry expectation:

$$\begin{aligned} \Omega_M^{\rm geom} &= 0.289 \pm 0.012 \\ \Omega_M^{\rm grow} &= 0.319 \pm 0.018 \\ w^{\rm geom} &= -1.11 \pm 0.06 \\ w^{\rm grow} &= -1.10 \pm 0.28 \end{aligned} \qquad (m_\nu \text{ marginalized over}). \tag{4.15}$$

The higher neutrino mass thus relieves the tension between geometry and growth. It is then of interest to show the value of m_ν favored by the data. The posterior probability on m_ν is shown in the right panel of Fig. 4.6. In the case where both Ω_M and w are split, $m_\nu = 0.45 \pm 0.21$ eV, higher than the fiducial value of $m_\nu = 0.06$ eV by ~ 2-σ. As a further test, constraints are placed on m_ν in the case of unsplit parameters (i.e. enforcing $\Omega_M^{\rm geom} = \Omega_M^{\rm grow}$ and $w^{\rm geom} = w^{\rm grow}$), obtaining $m_\nu = 0.45 \pm 0.12$ eV. This result is in good agreement with Reference [10], who find a similar mass at $m_\nu = 0.36 \pm 0.10$ eV using a combined BAO+RSD+Planck dataset. This higher value for the sum of neutrino masses would explain the preference of the growth probes for less growth of structure than predicted; higher-mass neutrinos act as warm dark matter, decreasing the overall formation of structure by dampening the amount of power in the matter power spectrum.

Fig. 4.4 and Eq. (4.12) show that the geometric equation of state is also somewhat incompatible with the ΛCDM value; the combined data mildly prefer a value $w^{\rm geom} = -1.13 \pm 0.06$. Most of the pull toward such negative values is found to be provided by the BAO. This fact, along with $w^{\rm grow} > -1$, exacerbates the disagreement between geometry and growth, leading to the 3.3σ incompatibility previously mentioned; growth however clearly exhibits the more pronounced tension with the standard value.

Finally, the Planck early-universe prior's effect on the combined constraints are investigated to see if it pushes the combined constraints away from the standard assumption that geometry=growth. To that effect, the Planck prior in Table 4.7 is replaced with the equivalent based on WMAP nine-year data [33]. While using this alternate EU prior, the data indicate that $w^{\rm geom} = -1.13 \pm 0.06$, $w^{\rm grow} = -0.78 \pm 0.08$, with $w^{\rm grow} > w^{\rm geom}$ now favored at 3.1σ (p-value=0.0017). These constraints are very similar to those obtained with the Planck EU prior, showing that the choice of prior does not affect the results appreciably.

4.7 Summary

In this chapter, I have performed a general test of the consistency of the wCDM cosmological model using current data from Type Ia Supernovae, CMB peak location, baryon acoustic oscillations, cluster counts, weak lensing shear two-point correlations, and redshift space distortions. The late universe DE parameters were split into those that describe the geometry of the universe and those that govern the growth of structure. Under the assumption of a ΛCDM universe, the parameters $\Omega_M^{\rm geom}$ and $\Omega_M^{\rm grow}$ were constrained (Fig. 4.3). Then, the more general model with the split equation of state parameters $w^{\rm geom}$ and $w^{\rm grow}$ was also considered, with constraints also placed on those parameters (Fig. 4.4). Several early universe parameters have been marginalized over for these results, as well as a number of nuisance parameters specific to

individual probes. The fiducial unsplit cases have also been constrained as a sanity check, with results shown in Fig. 4.2. The complementarity of the various probes is impressive, as seen in the constraints. The overall goodness-of-fit to the ΛCDM model is satisfactory, and the constraints on the split parameters are very tight (see Eqs. 4.10 and 4.12 and Table 4.8).

One surprise is the constraints from RSD, which are in $\simeq 3-\sigma$ conflict with wCDM. The RSD prefer less growth at late times than is predicted by the standard cosmological model, as is apparent in Fig. 4.4; this can also be seen in the RSD data in Fig. 4.1. As pointed out in Section 4.6, this tension has already been noticed in the literature. In the Discussion section, I demonstrate that the discrepancy remains at the still-significant 3.1σ once the most discrepant RSD measurement is replaced by one from an alternative analysis. The discrepancy may be resolved with a higher value of the neutrino mass sum than the minimum value predicted by current neutrino oscillation data under the assumptions of the normal hierarchy between the mass eigenstates, $m_\nu = 0.45 \pm 0.12$ eV; see Fig. 4.6. This higher value of the sum of neutrino masses would account for the suppressed growth favored by the RSD. However, systematics may also play a role in resolving the discrepancy; more work in this area is needed to determine which of these effects is responsible.

CHAPTER 5

Summary and Conclusions

As an explanation to the acceleration of the expansion of the universe, the dark energy paradigm with a cosmological constant, ΛCDM, has been tremendously successful. Time and time again, ΛCDM has withstood falsification from new data and become the leading candidate to explain this great mystery. Even though there have been many attempts at disproving ΛCDM, or replacing it with an alternate theory, it has survived, and even thrived, so far.

However, even with all of the information we have gathered using cosmological observations, the true nature of dark energy has remained a great mystery. And while the leading contender is that of the cosmological constant, many alternate models have been proposed which are still able to explain the acceleration of the universe's expansion, and many of these models have not yet been ruled out. Due to the open nature of dark energy, it is currently a very exciting time in dark energy cosmology.

In the previous chapters, we have seen the impressive constraining power of the current surveys. The maturing of new types of probes (several of which were described in Chapter 2), some which didn't exist a decade ago, and new more powerful surveys, have led many to call the current era a golden age of cosmology. The things learned over the past decade and a half have provided an abundance of new information and greatly increased the mapping of the expansion rate of the univere and the growth of cosmic structures, though perhaps not the understanding of the nature of dark

energy.

In Chapter 3 I illustrated explicitly the effects of SN systematics on the constraints of DE parameters. Future surveys will need to better control for these systematics, primarily calibration errors of the various instruments. The work by the SNLS team in quantifying the systematics is very important in this regard, and the hope is that future surveys will be able to reduce these sources of error significantly. Space-based telescopes, for example, will help in the reduction of calibration errors, primarily due to the lack of atmospheric effects which can affect the calibration.

Future surveys will also provide much better constraints on the growth of structure, which I showed in Chapter 4 were not as good as the constraints on geometry. The upcoming Dark Energy Spectroscopic Instrument (DESI) [51] will provide detailed spectra of a large number of objects ($\sim$30 million), and will therefore be particularly useful for the measuring the RSD and BAO. DESI will also provide detailed measurements of the Lyman-alpha forest, a recently-developed probe which will also provide details of the growth of structure, as well as information regarding the sum of neutrino masses.

Other surveys, such as the space-based Euclid [50] and Wide-Field Infrared Survey Telescope (WFIRST) [79] satellites, will provide deep measurements of the universe with their near-infrared sensors and high resolution imaging. Both Euclid and WFIRST will have the capability to measure the spectra of distant galaxies, which will provide detailed measurements of RSD and galaxy clustering. These surveys will cover large volumes of the sky (15,000 deg^2 for Euclid and 2400 deg^2 out to a redshift of almost $z = 3$ for WFIRST) and will reduce systematic uncertainties such as those due to atmospheric effects, which will be useful for differentiating between the various possible explanations for the lower-than-expected growth seen in the RSD by current surveys. The large survey volumes will also detect a large number of galaxies (Euclid, for example, is expected to observe around 10 billion galaxies), potential resulting in

tens of thousands of galaxy clusters and further placing much-needed constraints on the growth of structure.

The probe that offers the largest potential for improvement in the future, weak gravitational lensing, will greatly benefit from the upcoming Large Synoptic Survey Telescope (LSST) [54]. This ground-based telescope will cover about half of the sky (20,000 $\deg^2$) and will go very deep by revisiting each patch of the sky about 1000 times over a period of ten years. Its very high resolution camera (3200 megapixels) will take very fast detailed images of the universe with a 9.6 $\deg^2$ field of view using 6 bands, which should lead to good-quality photometric redshifts. This makes it perfectly suited for measurements of the weak lensing shear two-point correlation function and cluster counts. The LSST team also expects to measure tens of thousands of new type Ia supernovae, allowing for a big improvement in the constraints on dark energy parameters.

Along with the new surveys, further insights into the modelling of these growth probes needs to be done, particularly RSD. With a better understanding of the RSD, we can determine if there are new sources of systematic uncertainties, and better understand how neutrino masses affect the growth of structure. Reference [85], for example, tests various analytic models used for analyzing RSD data, and identifies challenges in modeling small-scale velocities. Finding models that better describe RSD is crucial to understanding possible sources of systematics in this cosmological probe, which in turn will allow for the better understanding of the role of neutrinos in the universe.

The current direction of research into dark energy is extremely exciting, with many recent advances in the field. Time will tell whether those advances eventually lead to the discovery of the true nature of dark energy, the realization of a new theory of gravity, or an option that has yet to be considered.

APPENDICES

APPENDIX A

Calculating the Equation of State Principal Components

A.1 Setting Up the Binned $w(z)$

Before calculating the Principal Components, $w(z)$ needs to be set up appropriately. Following the procedure by the Figure of Merit Science Working Group (FoMSWG), $w(z)$ is modeled as a piecewise constant function in bins of $\Delta a = 0.025$ for the range $0.1 \leq a \leq 1.0$, resulting in 36 bins [3]. The ith bin will contain the value $w_i = w(z_i), i = 0, 1, \ldots, 35$ for the interval between $a_i = 1 - 0.025i$ and $a_{i+1} = 1 - 0.025(i+1)$, or equivalently between $z_i = 0.025i/(1 - 0.025i)$ and $z_{i+1} = 0.025(i+1)/(1 - 0.025(i+1))$.

In this form, the DE term in Eq. (1.4) takes on the form [39]

$$\frac{\rho_{DE}(z)}{\rho_{\text{crit}}} = (1 - \Omega_M) \left(\frac{1+z}{1 + z_i - \Delta z_i/2} \right)^{3(1+w_i)} \times \prod_{j=1}^{i-1} \left(\frac{1 + z_j + \Delta z_j/2}{1 + z_j - \Delta z_j/2} \right)^{3(1+w_j)} \quad \text{(A.1)}$$

for z within the ith bin, $z_i \leq z \leq z_{i+1}$.

A.2 Calculating the Fisher Matrix

The Fisher Matrix formalism is used to create a covariance matrix for the parameters $\{p_i\} = \{\Omega_M, \mathcal{M}, \{w_i\}\}$ [1] For a given likelihood, the sharpness of that likelihood gives us information on how sensitive our model is to shifts in the parameter space, i.e. for a sharply peaked likelihood, a small change in any parameter greatly reduces the likelihood of the model defined by that new value, while for a broad likelihood, any small shift has small effects on the value of the likelihood of the relevant model. Thus, the amount a likelihood peaks, which is measured by its curvature, provides a measure of how useful a set of data will be in distinguishing different models. This brings us to the Fisher information matrix, or simply the Fisher matrix, defined as

$$\mathcal{F}_{ij} = \left\langle -\frac{\partial^2 \ln \mathcal{L}}{\partial p_i \partial p_j} \right\rangle, \tag{A.2}$$

where $\mathcal{L}$ is the likelihood. The Fisher matrix provides a quantitative measure of the effectiveness of a set of data's ability to constrain a set of cosmological parameters. The angle brackets ($\langle\rangle$) mean that an expectated value is calculated over realizations of the data, allowing us to find an analytic form for the expression. By assuming the likelihood $\mathcal{L}$ is a multivariate Gaussian

$$\mathcal{L} = \frac{1}{(2\pi)^{n/2} |\det C|^{1/2}} \exp\left[-\frac{1}{2} (d - \bar{d})_i^T C_{ij}^{-1} (d - \bar{d})_j \right] \tag{A.3}$$

where d_i are the data, $\bar{d}_i$ the expected value for that data point, and C_{ij} is the covariance of the data points, Eq. (A.2) can be simplified (after some algebra) to

$$\mathcal{F}_{ij} = \frac{1}{2} \mathrm{Tr}\left[C^{-1} \frac{dC}{dp_i} C^{-1} \frac{dC}{dp_j} \right] + \left(\sum_{m,n} \frac{\partial \langle d_m \rangle}{\partial p_i} C_{mn}^{-1} \frac{\partial \langle d_n \rangle}{\partial p_j} \right) \tag{A.4}$$

[1] For the purposes of creating the Fisher Matrix, only one value of $\mathcal{M}$ is used (as proposed in the FoMSWG parameterization [3]), though for the actual constraints, two are used.

where $\langle d_m \rangle$ is the expectation value for the mth data point, C_{mn} is the covariance between the mth and nth data points. All derivatives are evaluated at the fiducial values, which for this calculation are $\Omega_M = 0.25$, $\mathcal{M} = 25$, and $w_i = -1$. The vector of expectation values $\langle \mathbf{d} \rangle$ includes data from the 472 expected SNe magnitudes for the redshifts measured in the SNLS data compilation [18], the 7 expected values of the acoustic parameter for the redshifts measured by the various BAO surveys [8, 61, 12, 13, 70, 5], and the single CMB expectation value from WMAP7 [48].

A.3 Calculating the Principal Components

The Fisher matrix provides a way to estimate errors given a set of data, that is, to create forecasts. The goal of this excesise, however, is to obtain a basis for the equation of state that would allow us to order a set of uncorrelated coefficients in a way that gives us the most possible information. This set of basis vectors is called the principal components of the equation of state $w(z)$. To obtain them, we must first marginalize over any additional parameters (in this case, Ω_M and $\mathcal{M}$) to obtain a reduced Fisher matrix with only the information on the binned $w(z)$. Marginalizing involves inverting the original Fisher matrix, selecting the sub-matrix associated with the 36 values of w_i, and reinverting the resulting matrix. Once we have the $w(z)$ Fisher matrix, we can obtain the set of uncorrelated parameters by diagonalizing the resulting 36×36 matrix

$$\mathcal{F} = E^T \Lambda E. \tag{A.5}$$

where Λ is a diagonal matrix and E is an orthogonal matrix. The vector of uncorrelated parameters $\mathbf{A}$ is related to the binned equation of state vector by the expression

$$\mathbf{A} = E(\mathbf{w} + \mathbf{1}) \tag{A.6}$$

The rows of the orthogonal matrix E are the principal components $e_i(z)$, and form an orthonormal basis. Taking advantage of the orthogonality of E, we can rewrite the above equation to the commonly used form [58]

$$w(z_i) = -1 + \sum_{j=0}^{35} \alpha_j e_j(z_i), \tag{A.7}$$

where α_j are the elements of the vector $\mathbf{A}$. By having uncorrelated parameters, the coefficients can be ordered from best-measured to worst-measured. The associated eigenvalues λ_i (the elements of the diagonal matrix Λ) determine how well the coefficients α_i can be measured, i.e. $\sigma(\alpha_i) = \lambda_i^{-1/2}$. The PCs are ordered such that $\sigma(\alpha_0) \leq \sigma(\alpha_1) \leq \ldots \leq \sigma(\alpha_{35})$ [39]. Because the coefficients of the last PCs are measured especially poorly, only the first 10 PCs are used for the analysis [68].

Eq. (A.6) can also be rewritten in another familiar form [39]

$$\alpha_i = \sum_{j=0}^{36} (1 + w(z_j)) e_i(z_j). \tag{A.8}$$

It is trivial to calculate the values of α_i for the ΛCDM model ($w(z) = -1$); $\alpha_i = 0$. these values are adopted as the fiducial values for α_i. Any of the α_i coefficients held fixed during the analysis are assigned this value (i.e. the final 26),

APPENDIX B

The Markov Chain Monte Carlo Algorithm

B.1 MCMC Methodology

In many instances, when placing constraints from cosmological data, one has to deal with a large number of parameters. The conventional approach is to calculate the likelihood of all parameter combinations, and use these likelihoods to place the constraint contours, commonly referred to as the "brute force" or "grid search" method. In this method, the addition of a new parameter increases the number of calculations required to fully explore the parameter space geometrically, that is, the total calculation time scales as n^2 for n parameters. For a small number of parameters ($\sim 2-4$), this is usually not a problem. However, for any greater number of parameters, a typical scenario in cosmology, the calculation time quickly becomes unwieldy, potentially on the order of years, decades, or even centuries for larger n! Thus, a different algorithm is required to quickly and accurately place constraints without requiring extreme amounts of computation time.

The Markov Chain Monte Carlo (MCMC) method is a powerful tool that overcomes these problems. It has the advantage that the computation time scales linearly with the number of parameters (rather than geometrically), resulting in much faster calculation times. The simplest form of this algorithm, the Metropolis-Hastings algorithm [56, 30], goes as follows:

1. Calculate $\mathcal{L}(\mathbf{x}_i)$, the likelihood of a point $\mathbf{x}_i$ in the parameter space, and add this point to your chain.

2. Calculate $\mathcal{L}(\mathbf{t})$, the likelihood of a test point $\mathbf{t} = \mathbf{x}_i + \Delta\mathbf{x}$, where $\Delta\mathbf{x}$ is a small step from the original point.

3. If $\mathcal{L}(\mathbf{t}) > \mathcal{L}(\mathbf{x}_i)$, then move to the test point; $\mathbf{t} \rightarrow \mathbf{x}_{i+1}$. Repeat with this new point (go to step 1.)

4. If $\mathcal{L}(\mathbf{t}) < \mathcal{L}(\mathbf{x}_i)$, generate a random number $a \in [0, 1]$. If $a > \mathcal{L}(\mathbf{t})/\mathcal{L}(\mathbf{x}_i)$, move to the test point; $\mathbf{t} \rightarrow \mathbf{x}_{i+1}$. Otherwise, stay at the current point; $\mathbf{x}_i \rightarrow \mathbf{x}_{i+1}$. Repeat with this new point (go to step 1.)

After running the MCMC, the resulting chain is binned in parameter space, with the value within the bin being the number of times the parameter combination within that bin appears in the chain. This multidimensional grid of "counts" is treated as an estimate of the underlying posterior distribution, i.e. the "true" posterior distribution; bins with higher counts are interpreted as areas of parameter space with a higher likelihood.

B.2 Optimizing MCMCs

Due to the random nature of the MCMC algorithm, the resulting distribution is only an estimate of the underlying posterior, and thus less accurate than the brute force method of obtaining constraints, resulting in parameter constraints that are slightly off from their "true" values. However, this effect can be reduced by running the MCMC for a long enough period of time; one of the properties of MCMC methods is that the sample better estimates the underlying posterior as the number of steps in the chain increases. Obviously, running an MCMC for extremely long amounts of time, which would result a almost-perfectly accurate posterior estimation, somewhat

defeats the purpose of the algorithm. In order to know when the estimation is "good enough", a quantity known as the convergence criterion is calculated. To do this, multiple MCMC chains are run simultaneously, and certain properties of these chains are compared. In this work, the Gelman-Rubin convergence criterion [28]

$$\hat{R} = \frac{\frac{N-1}{N}W + B\left(1 + \frac{1}{M}\right)}{W} \tag{B.1}$$

is used, where the variance within the overall distribution is

$$W = \frac{1}{M(N-1)} \sum_{ij} (y_i^j - \bar{y}^j)^2, \tag{B.2}$$

and the variance between chains is

$$B = \frac{1}{M-1} \sum_{j=1}^{M} (\bar{y}^j - \bar{y})^2. \tag{B.3}$$

Here, N is the average length of the chains, M the number of chains, y_i^j is the ith element in the jth chain, and the quantities

$$\bar{y}^j = \frac{1}{N} \sum_i y_i^j \tag{B.4}$$

$$\bar{y} = \frac{1}{NM} \sum_{ij} y_i^j \tag{B.5}$$

are the mean of chain j and the mean of the entire distribution, respectively. Notice that as the length of the chain tends towards infinity, (which would result in the true posterior), the variance between chains would disappear (since they would all be the same); as such, the convergence criterion tends towards $\hat{R} = 1$ for longer chains. Thus, convergence criterions near $\hat{R} = 1$ are generally considered "good enough"; conservative values are typically those less than about $\hat{R} \leq 1.03$, while more stringent cases might prefer convergence criterions of $\hat{R} \leq 1.001$.

A good MCMC code will not only calculate the convergence of the chains, but will also be efficient: ideally, it will move from one point to the next with about a 1/3 chance, allowing for fast runs overall. The main way to do this is to know the general directions to step in, which can be specified with the eigenvectors of the covariance of the parameters, and the general step size in those directions, obtained from a Gaussian distribution where the standard deviation is determined by the eigenvalues of the covariance. These quantities can be obtained by running a few short MCMCs to "test" the underlying posterior and get some general properties. A Fisher matrix can also work well in this instance.

Finally, when beginning an MCMC, the initial point should be chosen at random. If this point is in an area of low likelihood, it is possible the MCMC will stay near the initial point during the beginning of the run, falsely indicating that the region has a higher likelihood value than in truth, leading to a "burn in" period. Therefore, it is prudent to discard the initial steps of the MCMC (say, the first 10%).

A great advantage of an MCMC is that once the chains have been computed, any postprocessing is relatively easy. This includes things like calculating the covariance of the parameters in the chain, binning the chain for plotting purposes, or any other type of analysis. In addition, marginalizing over any parameters is extremely simple: just ignore the columns associated with those parameters, no integrating required.

APPENDIX C

Details on the MaxBCG Dataset and Likelihood Calculation

C.1 Cluster Count and Mean Mass Data

The MaxBCG Cluster Catalog contains measurements of the number of galaxies within a galaxy cluster, referred to as a cluster's richness N_Δ, where Δ is the overdensity at which the radius of the cluster is determined (Reference [66] utilizes an overdensity of $\Delta = 200$ for their data points). The number of clusters within a given richness range has then been binned, the details of which can be seen in Table C.1 and in the top panel of Fig. C.1.

Richness bin	No. of Clusters
11-14	5167
14-18	2387
19-23	1504
24-29	765
30-38	533
39-48	230
49-61	134
62-78	59
79-120	31

Table C.1: The number of clusters with a richness within a given bin.

In addition to the binned richness data, there are five clusters with a richness

Richness bin	No. of Clusters	$\langle M_{200b}\rangle[10^{14}M_{\odot}]$
12-17	5651	1.298 ± 0.183
18-25	2269	1.983 ± 0.260
26-40	1021	3.846 ± 0.536
41-70	353	5.475 ± 0.766
71+	55	13.03 ± 2.01

Table C.2: Mean mass (and their number) of clusters with a richness within the given bin.The errors in the mass are added to the total covariance; see text for details.

$N_{200} = 126, 139, 156, 164, 188$. Clusters of richness $N_{200} > 120$ are rare, thus, these clusters are not analyzed using a Gaussian likelihood, but instead are added to the analysis on an individual basis using a Bernoulli (binary) distribution

$$P(N|N_{200}) = \begin{cases} 1-p & \text{if } N = 0 \\ p & \text{if } N = 1, \end{cases} \tag{C.1}$$

which is adequate as long as the probability that two clusters have the same richness is negligible. Here p is the probability that a cluster with a given richness will be found, or more explicitly $p = \langle N|N_{200}\rangle$. With this distribution, the likelihood of these five clusters is

$$\ln \mathcal{L}_{\rm tail} = \sum_{N_{200}>120} \langle N|N_{200}\rangle - \sum_{N_{200}=1} \left(\langle N|N_{200}\rangle + \ln\langle N|N_{200}\rangle\right). \tag{C.2}$$

The MaxBCG catalog also contains data of the mean masses of clusters within a given richness bin: these are summarized in Table C.2 and in the bottom panel of Fig. C.1. The mass of the clusters has been calibrated using weak gravitational lensing measurements from Reference [45]. These cluster masses have been measured under the assumption of a ΛCDM universe with $\Omega_M = 0.27$. Since variations on the cosmology are planned during analysis, the overdensity, which depends on the particular cosmology, would change to $\Delta = 200\ (0.27/\Omega_M)$. As such, the cluster

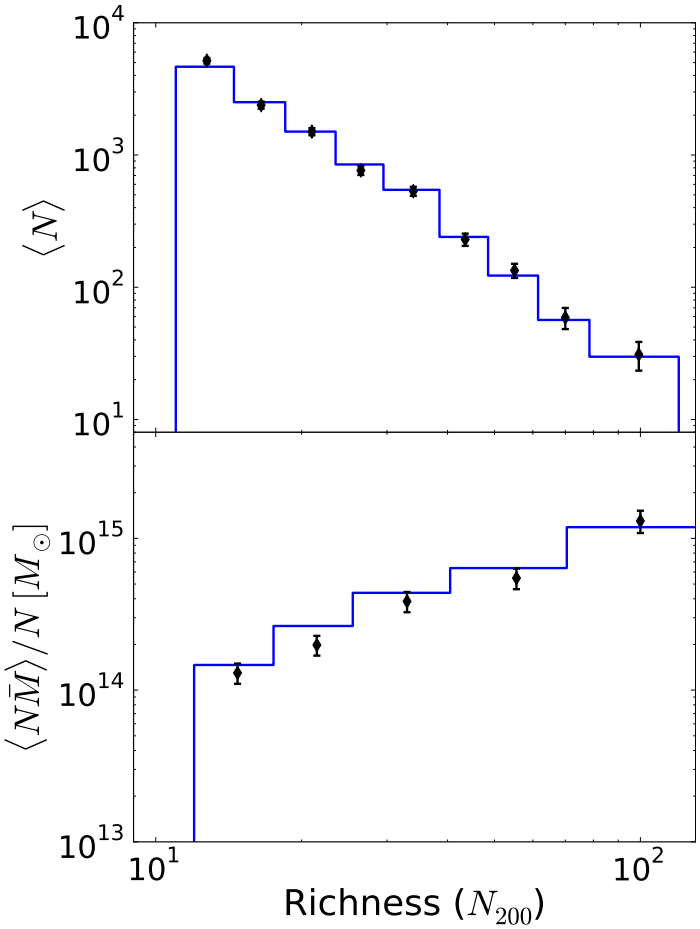

Figure C.1: Top: Number of galaxy clusters within a given richness bin in the MaxBCG dataset. Errors shown are the diagonal parts of the covariance matrix. The step function shown uses the parameter values from the best fit ΛCDM model (Column 2 of Table 4.8). The data are summarized in Table C.1. Bottom: Mean mass of galaxy clusters within the given richness bin in the MaxBCG dataset. The step function uses the same parameter values as the top figure. The data are summarized in Table C.2.

masses need to be rescaled back to an overdensity $\Delta = 200$. This can be achieved using the Hu and Kravstov equation for mass rescaling [37]

$$\frac{M_h}{M_v} = \frac{\Delta_h}{\Delta_v}\frac{1}{c^3}\left(\frac{r_h}{r_s}\right)^3 \tag{C.3}$$

where M_h is the mass of the halo, M_v is the virial mass, r_h is the radius of the halo given an overdensity, r_s the scale radius for an NFW profile, c is the concentration

factor, Δ_h is the overdensity used to define M_h, and Δ_v is the virial overdensity

$$\Delta_v \approx \frac{18\pi^2 + 82\left[\Omega_M(z) - 1\right] - 39\left[\Omega_M(z) - 1\right]^2}{\Omega_M(z)}. \tag{C.4}$$

The ratio of radii is given by

$$\frac{r_s}{r_h} = x\left(f_h = \frac{\Delta_v}{\Delta_h} f\left(\frac{1}{c}\right)\right) \tag{C.5}$$

where

$$f(x) = x^3\left[\ln(1 + x^{-1}) - (1 + x)^{-1}\right] \tag{C.6}$$

and its inverse is approximated as

$$x(f) = \left[a_1 f^{2p} + \left(\frac{3}{4}\right)^2\right]^{-1/2} + 2f. \tag{C.7}$$

Here $p = a_2 + a_3 \ln f + a_4 (\ln f)^2$, and $a_i = \{0.5116, -0.4283, -3.13 \times 10^{-3}, -3.52 \times 10^{-5}\}$. Finally, the concentration can be expressed in terms of the virial mass as

$$c(M_v) = 9(1 + z)^{-1}(M_v/M_*)^{-0.13} \tag{C.8}$$

where M_* is the critical mass and is calculated at the present day ($z = 0$).

C.2 Cluster Covariance Matrix

The covariance of the data is composed of five parts [66]. The first is the uncertainty due to shot noise, which take the form of Poisson fluctuations

$$(C_{a,a'})_P = \delta_{a,a'} \langle N \rangle. \tag{C.9}$$

These uncertainties are equal to the expectation values for each bin (see Section 2.5) and form a diagonal along the covariance. There are similar terms for the mean mass data points.

The second contribution to the covariance is the uncertainty due to sample variance: the smaller the sample of clusters, the more likely it is for that sample to not be fully representative of the total population. This uncertainty takes the form

$$(C_{a,a'})_S = \langle bN_a \rangle \langle bN_{a'} \rangle \sigma^2(V), \tag{C.10}$$

where V is the survey volume, $\sigma(V)$ is the amplitude of matter fluctuations for that volume, and

$$\langle bN_a \rangle = V \left[dM b(M) \frac{dn}{dM} \langle \psi_a | M \rangle \right]. \tag{C.11}$$

Here, $\langle \psi_a | M \rangle$ is the probability weighting function defined in Eq. (2.17) for bin a, dn/dM is the Tinker Halo Mass Function [80] as defined in Eq. 2.21, and $b(M)$ is the halo bias. Similar to Reference [66], the the Sheth-Torman halo bias is used [76]

$$b(M) = 1 + \frac{(a\nu - 1)}{\delta_c} + \frac{2p/\delta_c}{1 + (a\nu)^p}, \tag{C.12}$$

where $\delta_c = 1.686$ is the critical overdensity, $\nu = \delta_c^2/\sigma^2$, and $a = 0.707$ and $p = 0.3$ are fitting parameters. As before, there are similar terms for the mean mass data points, as well as the cross terms between number counts and mean masses.

The third contribution to the covariance matrix is errors due to the stochasticity of the mass-richness relation. This error leads to uncertainties in the precise mass binning of the cluster sample and takes the form

$$(C_{a,a'})_B = \int dM dz \frac{dn}{dM} \frac{dV}{dz} \langle \phi | z \rangle \left[\delta_{a,a'} \langle \psi_a | M \rangle - \langle \psi_a | M \rangle \langle \psi_{a'} | M \rangle \right], \tag{C.13}$$

with similar terms for the mean masses.

The fourth contribution to the covariance is measurement errors of the weak lensing mass $\Delta\langle M_{200b}\rangle$, which are shown in Table C.2 along with the mean mass values for each bin. These errors are multiplied by the number of clusters within the mean mass richness bins, and then added in quadrature to the diagonal elements of the five mass data points (but not to the nine number data points). Thus, this contribution has the form

$$(C_{a,a'})_M = \begin{cases} 0 & \text{if } a \text{ is a number count bin} \\ \delta_{a,a'}(N_a \Delta\langle M_{200b}\rangle_a)^2 & \text{if } a \text{ is a mean mass bin.} \end{cases} \tag{C.14}$$

The final contribution to the covariance is the uncertainty in the purity and completeness of the MaxBCG sample. If we define N_{true} as the number of clusters expected in the absence of systematics, the observed number of clusters N_{obs} is

$$N_{\text{obs}} = \lambda \; N_{\text{true}}, \tag{C.15}$$

where λ is a parameter that characterizes both the purity and completeness. It follows that

$$\text{Var}(N_{\text{obs}}) = \text{Var}(\lambda) \; \langle N_{\text{true}}\rangle^2 + \langle\lambda\rangle^2 \; \text{Var}(N_{\text{true}}). \tag{C.16}$$

A similar analysis can be done for the average mass within a richness bin

$$(N\bar{M})_{\text{obs}} = \tilde{\lambda} \; (N\bar{M})_{\text{true}} \tag{C.17}$$

where $\tilde{\lambda}$ is a different correction factor that takes into account the mass contribution to the purity and completeness. A difficulty arises in that we cannot know a priori what this correction factor is, however, Reference [66] argues that $\lambda = \tilde{\lambda} = 1 \pm 0.05$; thus $\text{Var}(\lambda) = \text{Var}(\tilde{\lambda}) = 0.05^2$. $\text{Var}(N_{\text{true}})$ is simply the terms in the covariance matrix discussed previously, so the final term for this part of the covariance matrix

is just

$$(C_{a,a'})_\lambda = \delta_{a,a'} \mathrm{Var}(\lambda) \langle N \rangle_a^2, \tag{C.18}$$

with similar terms for the mass expectations. Combining all of these contributions, we get the total covariance is

$$(C_{a,a'})_{\mathrm{tot}} = (C_{a,a'})_P + (C_{a,a'})_S + (C_{a,a'})_B + (C_{a,a'})_M + (C_{a,a'})_\lambda \tag{C.19}$$

C.3 Calculating the Cluster χ^2 Statistic

With the vector of observables and covariance matrix, we can construct the χ^2 statistic for clusters

$$\chi^2_{\mathrm{clusters}} = \left(\Delta \mathbf{x}^T (C_{\mathrm{tot}})^{-1} \Delta \mathbf{x}\right) - 2 \ln \mathcal{L}_{\mathrm{tail}}, \tag{C.20}$$

where $\Delta \mathbf{x} = \mathbf{x} - \langle \mathbf{x} | \mathbf{p} \rangle$, $\mathbf{x}$ is the vector of observables

$$\mathbf{x} = \{N_1, \ldots, N_9, (N\bar{M})_1, \ldots, (N\bar{M})_5\}, \tag{C.21}$$

and $\langle \mathbf{x} | \mathbf{p} \rangle$ is the corresponding expectation value given a set of parameters $\mathbf{p}$.

BIBLIOGRAPHY

[1] A. Abate and O. Lahav. The Three Faces of Ω_m: Testing Gravity with Low and High Redshift SN Ia Surveys. *MNRAS*, 389, Sept. 2008.

[2] A. Albrecht, G. Bernstein, R. Cahn, W. L. Freedman, J. Hewitt, et al. Report of the Dark Energy Task Force. *arXiv*, 0609591, 2006.

[3] A. J. Albrecht et al. Findings of the Joint Dark Energy Mission Figure of Merit Science Working Group. *arXiv*, 0901.0721, 2009.

[4] S. W. Allen, A. E. Evrard, and A. B. Mantz. Cosmological Parameters from Observations of Galaxy Clusters. *Ann.Rev.Astron.Astrophys.*, 49:409–470, 2011.

[5] L. Anderson, E. Aubourg, S. Bailey, D. Bizyaev, M. Blanton, et al. The clustering of galaxies in the SDSS-III Baryon Oscillation Spectroscopic Survey: baryon acoustic oscillations in the Data Release 9 spectroscopic galaxy sample. *MNRAS*, 427:3435–3467, Dec. 2012.

[6] R. Bean and M. Tangmatitham. Current constraints on the cosmic growth history. *Phys.Rev.*, D81:083534, 2010.

[7] J. Beringer et al. Review of Particle Physics (RPP). *Phys.Rev.*, D86:010001, 2012.

[8] F. Beutler, C. Blake, M. Colless, D. H. Jones, L. Staveley-Smith, et al. The 6dF Galaxy Survey: Baryon Acoustic Oscillations and the Local Hubble Constant. *Mon.Not.Roy.Astron.Soc.*, 416:3017–3032, 2011.

[9] F. Beutler, C. Blake, M. Colless, D. H. Jones, L. Staveley-Smith, et al. The 6dF Galaxy Survey: $z \approx 0$ measurement of the growth rate and σ_8. *Mon.Not.Roy.Astron.Soc.*, 423:3430–3444, 2012.

[10] F. Beutler et al. The clustering of galaxies in the SDSS-III Baryon Oscillation Spectroscopic Survey: Signs of neutrino mass in current cosmological datasets. *arXiv*, 1403.4599, 2014.

[11] F. Beutler et al. The clustering of galaxies in the SDSS-III Baryon Oscillation Spectroscopic Survey: Testing gravity with redshift-space distortions using the power spectrum multipoles. *Mon.Not.Roy.Astron.Soc.*, 443, Sept. 2014.

[12] C. Blake, S. Brough, M. Colless, C. Contreras, W. Couch, et al. The WiggleZ Dark Energy Survey: Joint measurements of the expansion and growth history at $z < 1$. *Mon.Not.Roy.Astron.Soc.*, 425:405–414, 2012.

[13] C. Blake, E. Kazin, F. Beutler, T. Davis, D. Parkinson, et al. The WiggleZ Dark Energy Survey: mapping the distance-redshift relation with baryon acoustic oscillations. *Mon.Not.Roy.Astron.Soc.*, 418:1707–1724, 2011.

[14] C. Cheng and Q.-G. Huang. The Dark Side of the Universe after Planck. *Phys.Rev.*, D89(4), Feb. 2014.

[15] M. Chevallier and D. Polarski. Accelerating universes with scaling dark matter. *Int. J. Mod. Phys.*, D10:213–224, 2001.

[16] N. Christensen, R. Meyer, L. Knox, and B. Luey. Ii: Bayesian methods for cosmological parameter estimation from cosmic microwave background measurements. *Class. Quant. Grav.*, 18:2677, 2001.

[17] C.-H. Chuang, F. Prada, F. Beutler, D. J. Eisenstein, S. Escoffier, et al. The clustering of galaxies in the SDSS-III Baryon Oscillation Spectroscopic Survey: single-probe measurements from CMASS and LOWZ anisotropic galaxy clustering. *arXiv*, 1312.4889, 2013.

[18] A. Conley et al. Supernova Constraints and Systematic Uncertainties from the First 3 Years of the Supernova Legacy Survey. *Astrophys.J.Suppl.*, 192:1, 2011.

[19] J. Dossett, J. Moldenhauer, and M. Ishak. Figures of merit and constraints from testing General Relativity using the latest cosmological data sets including refined COSMOS 3D weak lensing. *Phys.Rev.*, D84:023012, 2011.

[20] J. N. Dossett, M. Ishak, and J. Moldenhauer. Testing General Relativity at Cosmological Scales: Implementation and Parameter Correlations. *Phys.Rev.*, D84:123001, 2011.

[21] J. Dunkley, M. Bucher, P. G. Ferreira, K. Moodley, and C. Skordis. Fast and reliable Markov chain Monte Carlo technique for cosmological parameter estimation. *MNRAS*, 356:925–936, Jan. 2005.

[22] C. Dvorkin, M. Wyman, D. H. Rudd, and W. Hu. Neutrinos help reconcile Planck measurements with both Early and Local Universe. *arXiv*, 1403.8049, 2014.

[23] D. J. Eisenstein et al. Detection of the baryon acoustic peak in the large-scale correlation function of SDSS luminous red galaxies. *Astrophys.J.*, 633:560–574, 2005.

[24] D. J. Eisenstein and W. Hu. Power spectra for cold dark matter and its variants. *Astrophys.J.*, 511:5, 1997.

[25] T. Erben, H. Hildebrandt, L. Miller, L. van Waerbeke, C. Heymans, et al. CFHTLenS: the Canada-France-Hawaii Telescope Lensing Survey - imaging data and catalogue products. *MNRAS*, 433:2545–2563, Aug. 2013.

[26] J. Frieman, M. Turner, and D. Huterer. Dark Energy and the Accelerating Universe. *Ann.Rev.Astron.Astrophys.*, 46:385–432, 2008.

[27] J. A. Frieman, D. Huterer, E. V. Linder, and M. S. Turner. Probing dark energy with supernovae: Exploiting complementarity with the cosmic microwave background. *Phys.Rev.*, D67:083505, 2003.

[28] A. Gelman and D. Rubin. Inference from iterative simulation using multiple sequences. *Statistical Science*, 7:457–511, 1992.

[29] J. Guy, P. Astier, S. Baumont, D. Hardin, et al. SALT2: using distant supernovae to improve the use of type Ia supernovae as distance indicators. *Astron.Astrophys.*, 466:11–21, Apr. 2007.

[30] W. Hastings. Monte Carlo Sampling Methods Using Markov Chains and Their Applications. *Biometrika*, 57:97–109, 1970.

[31] C. Heymans, L. Van Waerbeke, L. Miller, T. Erben, et al. CFHTLenS: the Canada-France-Hawaii Telescope Lensing Survey. *MNRAS*, 427:146–166, Nov. 2012.

[32] M. Hicken et al. Improved Dark Energy Constraints from 100 New CfA Supernova Type Ia Light Curves. *Astrophys. J.*, 700:1097–1140, 2009.

[33] G. Hinshaw et al. Nine-Year Wilkinson Microwave Anisotropy Probe (WMAP) Observations: Cosmological Parameter Results. *Astrophys.J.Suppl.*, 208:19, 2013.

[34] A. Hojjati, L. Pogosian, and G.-B. Zhao. Detecting Features in the Dark Energy Equation of State: A Wavelet Approach. *JCAP*, 1004:007, 2010.

[35] A. Hojjati, G.-B. Zhao, L. Pogosian, A. Silvestri, R. Crittenden, et al. Cosmological tests of General Relativity: a principal component analysis. *Phys.Rev.*, D85:043508, 2012.

[36] Z. Hou, C. Reichardt, K. Story, B. Follin, R. Keisler, et al. Constraints on Cosmology from the Cosmic Microwave Background Power Spectrum of the 2500-square degree SPT-SZ Survey. *Astrophys.J.*, 782:74, 2014.

[37] W. Hu and A. V. Kravtsov. Sample variance considerations for cluster surveys. *Astrophys.J.*, 584:702–715, 2003.

[38] D. Huterer and A. Cooray. Uncorrelated estimates of dark energy evolution. *Phys. Rev.*, D71:023506, 2005.

[39] D. Huterer and G. Starkman. Parameterization of dark-energy properties: A principal- component approach. *Phys. Rev. Lett.*, 90:031301, 2003.

[40] D. Huterer and M. Takada. Calibrating the nonlinear matter power spectrum: Requirements for future weak lensing surveys. *Astroparticle Physics*, 23:369–376, May 2005.

[41] D. Huterer and M. S. Turner. Probing the dark energy: Methods and strategies. *Phys. Rev.*, D64:123527, 2001.

[42] M. Ishak, A. Upadhye, and D. N. Spergel. Probing cosmic acceleration beyond the equation of state: Distinguishing between dark energy and modified gravity models. *Phys.Rev.*, D74:043513, 2006.

[43] E. E. Ishida and R. S. de Souza. Hubble parameter reconstruction from a principal component analysis: minimizing the bias. *Astron.Astrophys.*, 527:A49, 2011.

[44] J. C. Jackson. A critique of Rees's theory of primordial gravitational radiation. *MNRAS*, 156:1P, 1972.

[45] D. E. Johnston et al. Cross-correlation Weak Lensing of SDSS galaxy Clusters II: Cluster Density Profiles and the Mass–Richness Relation. *arXiv*, 0709.1159, 2007. FERMILAB-PUB-07-720-A, SLAC-PUB-12813.

[46] A. Joyce, B. Jain, J. Khoury, and M. Trodden. Beyond the Cosmological Standard Model. *arXiv*, 1407.0059, June 2014.

[47] R. Kessler et al. First-year Sloan Digital Sky Survey-II (SDSS-II) Supernova Results: Hubble Diagram and Cosmological Parameters. *Astrophys. J. Suppl.*, 185:32–84, 2009.

[48] E. Komatsu et al. Seven-Year Wilkinson Microwave Anisotropy Probe (WMAP) Observations: Cosmological Interpretation. *Astrophys. J. Suppl.*, 192:18, 2011.

[49] L. M. Krauss and M. S. Turner. The Cosmological constant is back. *Gen.Rel.Grav.*, 27:1137–1144, 1995.

[50] R. Laureijs, J. Amiaux, S. Arduini, J. . Augueres, J. Brinchmann, R. Cole, M. Cropper, C. Dabin, L. Duvet, A. Ealet, and et al. Euclid Definition Study Report. *arXiv*, 1110.3193, Oct. 2011.

[51] M. Levi et al. The DESI Experiment, a whitepaper for Snowmass 2013. *arXiv*, 1308.0847, 2013.

[52] E. V. Linder. Exploring the expansion history of the universe. *Phys. Rev. Lett.*, 90:091301, 2003.

[53] E. V. Linder. Cosmic growth history and expansion history. *Phys. Rev.*, D72(4):043529–+, Aug. 2005.

[54] LSST Collaboration, A. Abate, et al. Large Synoptic Survey Telescope: Dark Energy Science Collaboration. *arXiv*, 1211.0310, Nov. 2012.

[55] N. MacCrann, J. Zuntz, S. Bridle, B. Jain, and M. R. Becker. Cosmic Discordance: Are Planck CMB and CFHTLenS weak lensing measurements out of tune? *ArXiv*, 1408.4742, Aug. 2014.

[56] N. Metropolis, A. Rosenbluth, M. Rosenbluth, A. Teller, and E. Teller. Equation of state calculations by fast computing machines. *J.Chem.Phys.*, 21:1087–1092, 1953.

[57] M. Mortonson, W. Hu, and D. Huterer. Figures of merit for present and future dark energy probes. *Phys. Rev.*, D82:063004, Sept. 2010.

[58] M. J. Mortonson, W. Hu, and D. Huterer. Falsifying paradigms for cosmic acceleration. *Phys. Rev.*, D79(2):023004–+, Jan. 2009.

[59] M. J. Mortonson, W. Hu, and D. Huterer. Testable dark energy predictions from current data. *Phys. Rev.*, D81:063007, Mar. 2010.

[60] N. Padmanabhan, X. Xu, D. J. Eisenstein, R. Scalzo, A. J. Cuesta, et al. A 2 per cent distance to z=0.35 by reconstructing baryon acoustic oscillations - I. Methods and application to the Sloan Digital Sky Survey. *Mon.Not.Roy.Astron.Soc.*, 427(3):2132–2145, 2012.

[61] W. J. Percival et al. Baryon Acoustic Oscillations in the Sloan Digital Sky Survey Data Release 7 Galaxy Sample. *Mon.Not.Roy.Astron.Soc.*, 401:2148–2168, 2010.

[62] S. Perlmutter et al. Measurements of omega and lambda from 42 high-redshift supernovae. *Astrophys. J.*, 517:565–586, 1999.

[63] Planck Collaboration, P. A. R. Ade, et al. Planck 2013 results. XVI. Cosmological parameters. *Astron.Astrophys.*, 2013.

[64] B. A. Reid, H.-J. Seo, A. Leauthaud, J. L. Tinker, and M. White. A 2.5space clustering of SDSS-III CMASS galaxies. *Mon.Not.Roy.Astron.Soc.*, 444:476–502, Oct. 2014.

[65] A. G. Riess et al. Observational evidence from supernovae for an accelerating universe and a cosmological constant. *Astron. J.*, 116:1009–1038, 1998.

[66] E. Rozo et al. Cosmological Constraints from the SDSS maxBCG Cluster Catalog. *Astrophys.J.*, 708:645–660, 2010.

[67] E. J. Ruiz and D. Huterer. Banana Split: Testing the Dark Energy Consistency with Geometry and Growth. *arXiv*, 1410.5832, Oct. 2014.

[68] E. J. Ruiz, D. L. Shafer, D. Huterer, and A. Conley. Principal components of dark energy with SNLS supernovae: the effects of systematic errors. *Phys.Rev.*, D86:103004, 2012. "Copyright (2012) by the American Physical Society.".

[69] L. Samushia, B. A. Reid, M. White, W. J. Percival, A. J. Cuesta, et al. The Clustering of Galaxies in the SDSS-III Baryon Oscillation Spectroscopic Survey (BOSS): measuring growth rate and geometry with anisotropic clustering. *Mon.Not.Roy.Astron.Soc.*, 439:3504–3519, Apr. 2014.

[70] A. G. Sanchez, C. Scoccola, A. Ross, W. Percival, M. Manera, et al. The clustering of galaxies in the SDSS-III Baryon Oscillation Spectroscopic Survey: cosmological implications of the large-scale two-point correlation function. *MNRAS*, 425:415–437, Sept. 2012.

[71] D. Scolnic, A. Rest, A. Riess, M. Huber, R. Foley, et al. Systematic Uncertainties Associated with the Cosmological Analysis of the First Pan-STARRS1 Type Ia Supernova Sample. *arXiv*, 1310.3824, Oct. 2013.

[72] M. Seikel, C. Clarkson, and M. Smith. Reconstruction of dark energy and expansion dynamics using Gaussian processes. *JCAP*, 1206:036, 2012.

[73] U. Seljak, A. Slosar, and P. McDonald. Cosmological parameters from combining the Lyman-alpha forest with CMB, galaxy clustering and SN constraints. *JCAP*, 0610:014, 2006.

[74] D. L. Shafer and D. Huterer. Chasing the phantom: A closer look at Type Ia supernovae and the dark energy equation of state. *Phys.Rev.*, D89:063510, 2014.

[75] A. Shafieloo, A. G. Kim, and E. V. Linder. Gaussian process cosmography. *Phys.Rev.*, D85:123530, 2012.

[76] R. K. Sheth and G. Tormen. An excursion set model of hierarchical clustering: ellipsoidal collapse and the moving barrier. *Mon.Not.Roy.Astron.Soc.*, 329:61–75, Jan. 2002.

[77] A. Silvestri, L. Pogosian, and R. V. Buniy. Practical approach to cosmological perturbations in modified gravity. *Phys.Rev.*, D87(10):104015, 2013.

[78] R. E. Smith, J. A. Peacock, A. Jenkins, S. D. M. White, C. S. Frenk, F. R. Pearce, P. A. Thomas, G. Efstathiou, and H. M. P. Couchman. Stable clustering, the halo model and non-linear cosmological power spectra. *MNRAS*, 341:1311–1332, June 2003.

[79] D. Spergel, N. Gehrels, J. Breckinridge, M. Donahue, A. Dressler, et al. Wide-Field InfraRed Survey Telescope-Astrophysics Focused Telescope Assets WFIRST-AFTA Final Report. *arXiv*, 1305.5422, May 2013.

[80] J. L. Tinker, A. V. Kravtsov, A. Klypin, K. Abazajian, M. S. Warren, et al. Toward a halo mass function for precision cosmology: The Limits of universality. *Astrophys.J.*, 688:709–728, 2008.

[81] R. A. Vanderveld, M. J. Mortonson, W. Hu, and T. Eifler. Testing dark energy paradigms with weak gravitational lensing. *Phys.Rev.*, D85:103518, 2012.

[82] S. Wang, L. Hui, M. May, and Z. Haiman. Is Modified Gravity Required by Observations? An Empirical Consistency Test of Dark Energy Models. *Phys.Rev.*, D76:063503, 2007.

[83] Y. Wang and M. Tegmark. Uncorrelated measurements of the cosmic expansion history and dark energy from supernovae. *Phys. Rev.*, D71:103513, 2005.

[84] D. H. Weinberg, M. J. Mortonson, D. J. Eisenstein, C. Hirata, A. G. Riess, and E. Rozo. Observational probes of cosmic acceleration. *Physical Reports*, 530:87–255, Sept. 2013.

[85] M. White, B. Reid, C.-H. Chuang, J. L. Tinker, C. K. McBride, et al. Tests of streaming models for redshift-space distortions. *arXiv*, 1408.5435, 2014.

[86] W. M. Wood-Vasey et al. Observational Constraints on the Nature of the Dark Energy: First Cosmological Results from the ESSENCE Supernova Survey. *Astrophys. J.*, 666:694–715, 2007.

[87] J.-Q. Xia, H. Li, and X. Zhang. Dark Energy Constraints after Planck. *Phys.Rev.*, D88:063501, 2013.

[88] O. Zahn and M. Zaldarriaga. Probing the Friedmann equation during recombination with future CMB experiments. *Phys.Rev.*, D67:063002, 2003.

[89] H. Zhan, L. Knox, and J. A. Tyson. Distance, Growth Factor, and Dark Energy Constraints from Photometric Baryon Acoustic Oscillation and Weak Lensing Measurements. *Astrophys.J.*, 690:923–936, 2009.

[90] G.-B. Zhao, R. G. Crittenden, L. Pogosian, and X. Zhang. Examining the Evidence for Dynamical Dark Energy. *Physical Review Letters*, 109(17):171301, Oct. 2012.

[91] G.-B. Zhao, T. Giannantonio, L. Pogosian, A. Silvestri, D. J. Bacon, et al. Probing modifications of General Relativity using current cosmological observations. *Phys.Rev.*, D81:103510, 2010.

[92] G.-B. Zhao, D. Huterer, and X. Zhang. High-resolution temporal constraints on the dynamics of dark energy. *Phys. Rev.*, D77:121302, 2008.

[93] G.-B. Zhao, H. Li, E. V. Linder, K. Koyama, D. J. Bacon, et al. Testing Einstein Gravity with Cosmic Growth and Expansion. *Phys.Rev.*, D85:123546, 2012.

[94] C. Zunckel and R. Trotta. Reconstructing the history of dark energy using maximum entropy. *Mon. Not. Roy. Astron. Soc.*, 380:865, 2007.